Regulation of autism-relevant behaviors by cerebellar-prefrontal cortical circuits

Elyza Kelly, Fantao Meng, Hirofumi Fujita, Felipe Morgado, Yasaman Kazemi, Laura Rice, Chongryu Ren, Christine Ochoa Escamilla, Jennifer Gibson, Sanaz Sajadi, et al.

HHS Public Access

Author manuscript

Nat Neurosci. Author manuscript; available in PMC 2021 January 13.

Published in final edited form as:

Nat Neurosci. 2020 September ; 23(9): 1102–1110. doi:10.1038/s41593-020-0665-z.

Regulation of autism-relevant behaviors by cerebellar–prefrontal cortical circuits

Elyza Kelly[1,2], **Fantao Meng**[1], **Hirofumi Fujita**[3], **Felipe Morgado**[4,5], **Yasaman Kazemi**[1], **Laura C. Rice**[6], **Chongyu Ren**[1], **Christine Ochoa Escamilla**[1], **Jennifer M. Gibson**[1,2], **Sanaz Sajadi**[1], **Robert J. Pendry**[2], **Tommy Tan**[1], **Jacob Ellegood**[5], **M. Albert Basson**[7], **Randy D. Blakely**[8], **Scott V. Dindot**[9], **Christelle Golzio**[10], **Maureen K. Hahn**[8], **Nicholas Katsanis**[11], **Diane M. Robins**[12], **Jill L. Silverman**[13], **Karun K. Singh**[14], **Rachel Wevrick**[15], **Margot J. Taylor**[16], **Christopher Hammill**[5], **Evdokia Anagnostou**[17], **Brad E. Pfeiffer**[2], **Catherine J. Stoodley**[6], **Jason P. Lerch**[4,5,18], **Sascha du Lac**[3], **Peter T. Tsai**[1,2,19,*]

[1.]Department of Neurology and Neurotherapeutics, University of Texas Southwestern Medical Center, Dallas, TX, USA

[2.]Department of Neuroscience, University of Texas Southwestern Medical Center, Dallas, TX, USA

[3.]Departments of Otolaryngology-Head and Neck Surgery, Neurology and Neuroscience, Johns Hopkins University School of Medicine, Baltimore, MD, USA

[4.]Department of Medical Biophysics, University of Toronto, Toronto, ON, Canada

[5.]Mouse Imaging Centre, Toronto Hospital for Sick Children, Toronto, ON, Canada

[6.]Department of Neuroscience, Center for Behavioral Neuroscience, American University, Washington, DC, USA

[7.]Centre for Craniofacial and Regenerative Biology and MRC Centre for Neurodevelopmental Disorders, King's College London, London, UK

[*]**Corresponding author**: correspondence to Peter T. Tsai.

Contributions

E.K., F. Meng, H. F., J.P.L., S.d.L. and P.T.T. formulated experiments and analysis. E.K., F. Meng, H.F., Y.K., C.O.E., J.M.G., S.S., C.R., D.J., R.P., T.T. and B.E.P. performed experiments and analysis. F. Morgado, J.E. and J.P.L. carried out the mouse structural imaging experiments and analysis. F. Morgado, J.E., M.J.T, C.H., E.A. and J.P.L. carried out the human structural imaging experiments and analysis. L.C.R. and C.J.S. performed functional imaging in humans and analysis of these studies. M.A.B., R.D.B., S.D., C.G., M.K.H., N.K., D.M.R., J.L.S, K.K.S. and R.W. provided critical reagents. E.K., H.F., J.P.L., S.d.L. and P.T.T. prepared the manuscript.

Ethics declarations

The authors declare no competing interests.

Additional information

Peer review information *Nature Neuroscience* thanks Ted Abel, Sarah Ferri and the other, anonymous, reviewer(s) for their contribution to the peer review of this work.

Data availability

The authors confirm that all relevant non-MRI data are included in the paper and/or its supplementary information files. Raw MRI data that support the findings of this study are available from the corresponding author upon reasonable request.

Code availability

All code is publicly available on GitHub (https://github.com/Mouse-Imaging-Centre/RMINC) or is available upon reasonable request.

[8]Department of Biomedical Science, Charles E. Schmidt College of Medicine and Brain Institute, Florida Atlantic University, Jupiter, Florida, USA

[9]Department of Veterinary Pathobiology, College of Veterinary Medicine & Biomedical Sciences, Texas A&M University, College Station, TX, USA

[10]Institut de Génétique et de Biologie Moléculaire et Cellulaire; Centre National de la Recherche Scientifique; Institut National de la Santé et de la Recherche Médicale; Université de Strasbourg, Illkirch, France

[11]ACT-GeM, Department of Human Genetics at Stanley Manne Children's Research Institute; Department of Pediatrics and Cellular and Molecular Biology, Northwestern University Feinberg School of Medicine, Chicago, IL, USA

[12]Department of Human Genetics, University of Michigan Medical School, Ann Arbor, MI, USA

[13]MIND Institute and Department of Psychiatry and Behavioral Sciences, University of California, Davis, Davis, CA, USA

[14]Department of Biochemistry and Biomedical Sciences, McMaster University, Hamilton, ON, Canada

[15]Department of Medical Genetics, University of Alberta, Edmonton, AB, Canada

[16]Department of Medical Imaging and Psychology, University of Toronto; Diagnostic Imaging, Hospital for Sick Children, Toronto, ON, USA

[17]Department of Pediatrics, University of Toronto, Holland Bloorview Kids Rehabilitation Hospital, Toronto, ON, USA

[18]Wellcome Centre for Integrative Neuroimaging, FMRIB, Nuffield Department of Clinical Neuroscience, University of Oxford, Oxford, UK

[19]Departments of Psychiatry and Pediatrics, University of Texas Southwestern Medical Center, Dallas, TX, USA

Abstract

Cerebellar dysfunction has been demonstrated in autism spectrum disorders (ASDs); however, the circuits underlying cerebellar contributions to ASD-relevant behaviors remain unknown. In this study, we demonstrated functional connectivity between the cerebellum and the medial prefrontal cortex (mPFC) in mice; showed that the mPFC mediates cerebellum-regulated social and repetitive/inflexible behaviors; and showed disruptions in connectivity between these regions in multiple mouse models of ASD-linked genes and in individuals with ASD. We delineated a circuit from cerebellar cortical areas Right crus 1 (Rcrus1) and posterior vermis through the cerebellar nuclei and ventromedial thalamus and culminating in the mPFC. Modulation of this circuit induced social deficits and repetitive behaviors, whereas activation of Purkinje cells (PCs) in Rcrus1 and posterior vermis improved social preference impairments and repetitive/inflexible behaviors, respectively, in male PC-*Tsc1* mutant mice. These data raise the possibility that these circuits might provide neuromodulatory targets for the treatment of ASD.

Main

ASDs are prevalent neurodevelopmental disorders characterized by social impairment and repetitive/inflexible behaviors. Increasing evidence has implicated cerebellar dysfunction in ASD1,2,3,4, and PC-specific deletion of *Tsc1* is sufficient to generate ASD-relevant social impairment and repetitive/inflexible behaviors in mice5. Many studies have detailed volumetric changes in the posterior cerebellar vermis and in Rcrus1 in children with ASD, and the degree of volumetric differences in these areas correlates with ASD symptom severity6,7. We recently demonstrated that inhibition of Rcrus1 PCs could generate both social impairments and repetitive behaviors, whereas stimulation of Rcrus1 PC function could rescue only social behaviors in PC-*Tsc1* mutant mice. The lack of reduction in repetitive/inflexible behaviors raised the possibility that additional cerebellar domains might regulate these behaviors8.

Additionally, the circuits connecting the cerebellum to other brain areas to orchestrate complex behaviors such as those altered in ASDs remain unknown. Polysynaptic connections between the cerebellum and the cortex have been demonstrated both in anatomic tracing studies and functional connectivity studies9,10,11,12,13. One cortical area shown to be involved in social behaviors14 and highly implicated in ASDs is the mPFC15. Changes in cerebellar–mPFC functional connectivity have also been identified in ASD1,16, in mouse models of cerebellar PC loss, and in genetic mouse models of ASD17,18. Rcrus1 is functionally connected with the contralateral mPFC in humans8,19, and disruptions in cerebellar–mPFC connectivity have been demonstrated in ASD20. Thus, we hypothesized that cerebellar–mPFC connections might play important roles in the regulation of ASD-relevant behaviors.

Results

Decreased PC function in PC-*Tsc1* mutant mice results in increased mPFC activity

To determine if cerebellar dysfunction affects mPFC activity, we examined the effect of *Tsc1* mutation in PCs (PC-*Tsc1* mutant mice5) on mPFC activity. We hypothesized that reduced inhibitory output from the mutant cerebellum would result in increased downstream mPFC activity, which would be consistent with previous studies showing that ASD mouse models display elevated mPFC activation in response to social interaction21 and that elevations in mPFC excitatory activity result in social deficits22,23. We performed extracellular single-unit recordings in anesthetized animals and found elevated single-unit firing frequency in the left prelimbic (PRL) mPFC of PC-*Tsc1* mutant mice (Fig. 1a and Extended Data Fig. 10). To confirm these findings, we performed in vivo recordings in awake, freely moving animals and found similar elevated single-unit firing frequency in these mutant mice (Extended Data Fig. 1). Acute mPFC slice recordings, to assess potential local synaptic and circuit changes, revealed decreased frequency of miniature inhibitory postsynaptic currents (mIPSCs) and increased mIPSC rise times in addition to reduced miniature excitatory synaptic current (mEPSC) amplitudes in slices from PC-*Tsc1* mice (Extended Data Fig. 2).

Inhibition of mPFC improves social deficits and repetitive/inflexible behaviors in PC-*Tsc1* mutant mice

Based on these data and earlier findings that decreasing mPFC excitatory activity can rescue social deficits in an ASD mouse model24, we evaluated whether chemogenetic reduction of left mPFC activity would be sufficient to reduce ASD-related behaviors in PC-*Tsc1* mutant mice. In vivo single-unit recordings in the PRL confirmed successful suppression of mPFC activity by chemogenetic inhibition (Gi with clozapine-N-oxide (CNO)) of the mPFC (Fig. 1b,c, Extended Data Fig. 1 and Supplementary Tables 1, 2 and 5). We then examined whether mPFC inhibition would affect social dysfunction in PC-*Tsc1* mutant mice. Behavioral experiments were conducted on male mice beginning at 7 weeks of age. PC-*Tsc1* mutant mice expressing green fluorescent protein (GFP) and vehicle (VEH)-injected PC-*Tsc1* mutant mice expressing Gi demonstrated no social preference in social approach paradigms, consistent with social impairments observed previously in PC-*Tsc1* mutants5. By contrast, PC-*Tsc1* mutant mice with chemogenetic inhibition of the left PRL did show a preference for a conspecific over an empty cup (Fig. 1d and Extended Data Fig. 1). Moreover, inhibition of the mPFC in PC-*Tsc1* mutant mice induced social novelty preference and preference for social over non-social odors (Fig. 1e,f and Extended Data Fig. 1). Furthermore, inhibition of the left mPFC reduced repetitive grooming in PC-*Tsc1* mutant mice compared to control (VEH- or GFP-injected) cohorts (Fig. 1g). Inhibition of mPFC activity also significantly improved flexibility in the water Y-maze reversal task (Fig. 1h). Motor learning, locomotor and anxiety behaviors were unaffected in PC-*Tsc1* mutants and not altered by mPFC chemogenetic inhibition (Extended Data Fig. 1). Taken together, these data demonstrate that inhibition of mPFC was sufficient to enhance social behavior and reduce repetitive grooming in PC-*Tsc1* mutants.

Rcrus1 and left mPFC connections are disrupted in mouse models of ASD-linked genes and in ASD

We and others previously demonstrated connectivity between the left mPFC and Rcrus1 in humans and primates8,9,10. To confirm functional connectivity between Rcrus1 and mPFC in mice, we first performed in vivo single-unit recordings in the left PRL mPFC with Cre-dependent inhibition (DIO Gi) of Rcrus1 in anesthetized mice with PC-specific expression of Cre recombinase (PC^{Cre}). Compared to control cohorts (VEH-treated and GFP-injected littermate cohorts), inhibition of Rcrus1 PCs increased the firing frequency of single units recorded from the left PRL mPFC (Fig. 2a), without altering unit firing frequency in the motor cortex or in the right PRL (Extended Data Fig. 3). Inhibition of cerebellar Rcrus1 induced a similar increase in firing frequency in the left PRL in awake mice (Extended Data Fig. 3). These data indicate that functional connectivity exists between Rcrus1 and the PRL and, consistent with PC inhibitory output, that decreased Rcrus1 PC activity leads to increased left PRL mPFC activity.

We hypothesized that connectivity between Rcrus1 and the left PRL mPFC might be disrupted in ASD mouse models and individuals with ASD. We first used structural covariance to examine a cohort of 94 mouse lines with mutations in ASD-linked genes (Supplementary Table 3). Structural covariance is a structural magnetic resonance imaging (MRI)-based technique that has been demonstrated to mirror findings of connectivity from

functional or diffusion MRI studies8,25. Sex and interaction with sex were included as covariates in the structural covariance model. We identified disrupted structural covariance between Rcrus1 and the left PRL mPFC in ASD models compared to littermate control cohorts, suggesting that altered Rcus1–mPFC connectivity might contribute to behavioral alterations in multiple genetic mouse models of ASD (false discovery rate (FDR) $q = 0.0191$; Supplementary Table 3). Because of the phenotypic and genetic heterogeneity of ASD, we then evaluated whether cerebellar–mPFC connectivity might be disrupted specifically in a subset of these models. We identified 30 of 94 models that displayed significant ($P < 0.05$) volume changes in the cerebellum and mPFC, a much larger number than would be expected by chance (the chance that 30 of 94 models would be observed as significant ($P < 0.05$) is $P = 2.02 \times 10^{-18}$ by binomial probability analysis). When considered together, these models show an even greater alteration in structural covariance ($q < 0.0001$) between Rcrus1 and the left mPFC compared to control littermate cohorts (Fig. 2b and Supplementary Table 3). Considering the altered structural covariance between these two regions in these mouse models, we assessed whether changes in structural covariance could also be detected in a large human cohort from the Province of Ontario Neurodevelopmental Disorders (POND) network26. Indeed, in directed region-of-interest comparisons using Rcrus1 as the seed, we identified significant ($P = 0.012$) disruption in structural covariance between Rcrus1 and the left rectus gyrus (Fig. 2c and Supplementary Table 4). The significance of this finding, however, did not survive testing for multiple corrections ($q > 0.05$). A regression model tested covariates for scanner, age at scan and sex. Further support for disruptions of connectivity in ASD was identified using group multivariate pattern analysis (MVPA) on resting-state functional MRI from a small cohort of male individuals with ASD compared to an age-matched, typical developing (TD) male cohort. This analysis revealed alterations in functional connectivity with the mPFC and Rcrus1 Rcrus2 in individuals with ASD ($P < 0.001$, FDR $q < 0.05$; Fig. 2d). Post hoc seed-to-voxel analysis from these regions showed significant reductions in functional connectivity between this cerebellar region of interest and the mPFC ($P < 0.001$, $k > 50$; Fig. 2e), including the region identified in both MVPA and structural imaging studies. Together, these data point to disruptions in connectivity between the mPFC and Rcrus1 both in mouse models and in humans with ASD.

Inhibition of mPFC improves social deficits and repetitive/inflexible behaviors induced by inhibition of Rcrus1 PCs

We thus hypothesized that Rcrus1 dysfunction might contribute to ASD-related behaviors by regulating mPFC activity. As PC-*Tsc1* mutant mice display increased mPFC activity, and inhibition of Rcrus1 also results in increased mPFC activity, we tested whether decreasing mPFC activity could rescue deficits induced by disruptions in Rcrus1 function. PC^{Cre} mice were injected with adeno-associated virus (AAV) containing DIO-Gi into Rcrus1 (Extended Data Fig. 3). These mice then received either AAV-Gi (hereafter referred to as Gi/Gi) or AAV-GFP (Gi/GFP) into the left PRL mPFC (Fig. 2f). Inhibition of the mPFC was confirmed by single-unit recordings (Extended Data Fig. 3). VEH-injected Gi/Gi and Gi/GFP mice exhibited significant social preference and social novelty preference, consistent with their control background. However, CNO-injected Gi/GFP mice demonstrated impairments in these behaviors as well as in social odor preference, consistent

with previous studies demonstrating social impairment with Rcrus1 PC inhibition (Fig. 2g–i and Extended Data Fig. 3)8. In contrast to these mice, CNO-injected Gi/Gi mice demonstrated normal social preference behaviors in all these tests (Fig. 2g–i and Extended Data Fig. 3). We then tested repetitive/inflexible behaviors. CNO-injected Gi/GFP mice showed increased repetitive grooming and impaired performance on the water T-maze reversal task, consistent with our previous studies (Fig. 2j,k)8. In contrast, CNO-treated Gi/Gi mice demonstrated no abnormal grooming nor impairments in reversal learning in the water Y-maze (Fig. 2j,k). Testing for locomotor, motor learning and anxiety behaviors showed no phenotypes that would alter the interpretation of the above findings (Extended Data Fig. 3). Taken together, these data indicate that reduction of mPFC activity is sufficient to rescue both social deficits and repetitive/inflexible behaviors induced by Rcrus1 PC inhibition and that the mPFC thus acts downstream of cerebellar Rcrus1 in the regulation of these ASD-relevant behaviors.

The cerebellar lateral nucleus regulates social behaviors

The above data indicate a role for Rcrus1–mPFC connections in the regulation of ASD-relevant behaviors; however, the precise circuit involved remains unknown. Because inhibitory PC output emerges from the cerebellum via cerebellar nuclei (CN), we identified the CN receiving Rcrus1 PC output. PC^{Cre} mice injected with DIO-Gi-mCherry into Rcrus1 showed targeting of the lateral/dentate nucleus (LN) (Fig. 3a), consistent with previous studies27. Additionally, we found that chemogenetic inhibition of LN (Extended Data Fig. 4) decreased the firing frequency of single units in the mPFC (Fig. 3b).

To further support a role for the LN in mediating ASD-relevant behaviors, we examined whether chemogenetic inhibition (Gi) of LN could ameliorate behavioral phenotypes in PC-*Tsc1* mutant mice (Fig. 3c and Extended Data Fig. 4). PC-*Tsc1* mice injected with AAV-GFP (VEH or CNO) or Gi (VEH) into the right LN showed no significant social preference, consistent with their mutant backgrounds. However, with chemogenetic inhibition of the right LN, the mutant mice demonstrated significant preference in social approach, social novelty and social olfaction testing (Fig. 3d–f and Extended Data Fig. 4). These data demonstrate that modulation of LN activity is sufficient to rescue social deficits in PC-*Tsc1* mutant mice. By contrast, neither repetitive behaviors nor behavioral flexibility were rescued by chemogenetic inhibition of the right LN (Fig. 3g,h), consistent with the previously observed absence of rescue upon stimulation of Rcrus1 (ref. 8). No significant differences between groups were observed for anxiety, locomotor and motor learning behaviors (Extended Data Fig. 4). Taken together, these findings are consistent with the LN mediating Rcrus1 rescue of social behaviors.

Optogenetic activation of ventromedial thalamic terminals in the mPFC induces ASD-related behaviors

To further delineate the circuit connecting Rcrus1 and mPFC, we examined pathways by which LN could connect to the left PRL mPFC. After injections of AAV-1^{Cre} into the right LN of Cre-dependent Td-tomato reporter mice for anterograde trans-synaptic tracing (Fig. 4a and Extended Data Fig. 5)28, we identified reporter expression in neuronal somata within the left thalamus and cortex postsynaptic to the right LN (Fig. 4b). Downstream thalamic

and cortical areas identified are consistent with previously published results (Extended Data Fig. 5)13,29. Thalamocortical projections from these neurons were evident from many terminals in layer 1 of the left PRL mPFC (Fig. 4c,d). The localization of terminals to this layer pointed us to the ventromedial (VM) thalamus as a mediator of LN–mPFC connections, as previous studies have demonstrated that inputs from the VM thalamus target layer 1 (ref. 30). Thus, we hypothesized that VM thalamus–PRL mPFC circuits might mediate Rcrus1-regulated ASD-relevant behaviors.

To test this hypothesis, we used an optogenetic approach to modulate activity of VM thalamic terminals in the left PRL mPFC. To examine whether activation of VM thalamic terminals in the mPFC was sufficient to generate ASD-relevant behavioral impairments, channelrhodopsin (ChR2) or GFP was introduced via viral injection into the VM thalamus of controls, and an optical fiber was placed over the left PRL mPFC (Fig. 4e,f and Extended Data Fig. 6). Acute slice recordings in the VM thalamus revealed activation upon laser stimulation (Fig. 4g). ChR2 activation of VM terminals in the left mPFC also resulted in increases in single-unit firing frequency in the left PRL with two different laser stimulation frequencies: 20 Hz and 4 Hz (Fig. 4h). To address the possibility that stimulation of VM thalamic terminals in the mPFC might cause anti-dromic effects on other cortical targets of the VM thalamus, we recorded single-unit firing frequency in the VM thalamus-targeted parietal association cortex during stimulation of VM thalamic terminals in the mPFC but did not observe any change in frequency (Extended Data Fig. 6).

Laser stimulation of 20 Hz and 4 Hz as well as laser-OFF conditions were used during behavioral testing. Twenty Hz was chosen to be consistent with previous studies in the mPFC23, whereas 4 Hz was chosen to more closely model previously published thalamic firing rates31. With light OFF or GFP injection (light OFF or ON), mice demonstrated significant social preference, consistent with the animals' control background; by contrast, 20-Hz or 4-Hz optical stimulation of VM terminals in the mPFC during social approach, novelty and olfaction tests induced social preference impairments in mice with viral-mediated expression of ChR2 in the VM thalamus (Fig. 4i–k and Extended Data Fig. 6). The photostimulation also induced repetitive grooming (Fig. 4l). We did not observe any effects of laser stimulation on locomotor behavior, motor learning or anxiety measures that would affect the interpretation of the social or grooming behaviors (Extended Data Fig. 6). Taken together, photo-activation of VM terminals in the left PRL mPFC was sufficient to induce social deficits and repetitive grooming.

Optogenetic silencing of VM thalamic terminals in the left PRL mPFC reduces ASD-relevant behaviors in PC-*Tsc1* mutants

We then evaluated whether inhibition of this VM thalamus–mPFC pathway is sufficient to rescue social deficits and repetitive behaviors in PC-*Tsc1* mutant mice. PC-*Tsc1* mutant mice had AAV-Archaerhodopsin (Arch) or GFP injected into the left VM thalamus, and an optical fiber was placed over the left PRL mPFC (Fig. 4m). Acute slice recordings revealed that Arch inhibited firing of VM thalamic neurons (Fig. 4n), and in vivo extracellular recordings showed that laser ON decreased mPFC single-unit firing in left PRL frequency (Fig. 4o). In vivo, GFP-control and light-OFF Arch-expressing PC-*Tsc1* mutants showed

social impairments consistent with their mutant backgrounds. By contrast, photo-inhibition of VM thalamus terminals in the left mPFC during social approach, novelty and olfaction tests increased social preference in Arch-expressing PC-*Tsc1* mutants (Fig. 4p–r and Extended Data Fig. 7). It also reduced grooming behavior in these mice compared to light-OFF or GFP-injected controls (Fig. 4s). The photo-inhibition did not induce any change in locomotion, motor learning or anxiety (Extended Data Fig. 7). These results demonstrate that inhibition of VM thalamus–PRL mPFC projections was sufficient to rescue both social impairments and repetitive grooming in PC-*Tsc1* mutant mice.

A polysynaptic circuit connects cerebellar vermis with mPFC via VM thalamus

We have demonstrated that inhibition of the PRL mPFC itself or its inputs from the VM thalamus both reduces repetitive grooming and increases social preference in PC-*Tsc1* mutant mice. In contrast, modulation of Rcrus1 or LN rescued only the social preference behaviors but did not affect grooming. We hypothesized that modulation of an additional cerebellar domain that regulates VM thalamic–mPFC circuits might be sufficient to rescue the repetitive grooming seen in PC-*Tsc1* mutants.

One cerebellar domain that has been implicated in ASD is the posterior cerebellar vermis6,7,32. Alterations in posterior vermis volume correlate with repetitive behaviors6,33 We first examined whether the posterior vermis is functionally connected to the mPFC. Indeed, we found that single-unit firing frequencies in the left PRL mPFC increased upon chemogenetic inhibition of vermis PCs (Fig. 5a). In addition, structural covariance MRI revealed significant alterations between posterior vermis and left PRL mPFC in our cohort of genetic ASD models when compared to control littermate cohorts (Fig. 5b, Extended Data Fig. 8 and Supplementary Table 3). To evaluate the anatomic circuitry mediating posterior vermis–mPFC connectivity, we identified which CN is targeted by the posterior vermis. Consistent with previous literature34, PCs projected predominantly to the medial/fastigial nucleus (MN, Fig. 5c). Injecting the MN and the LN with different fluorescent AAV markers revealed that both nuclei provide axon terminals into the left VM thalamus (Fig. 5d,e and Extended Data Fig. 9). Additionally, AAV-1^{Cre} expression in the MN of Cre-dependent Td-tomato reporter mice labels postsynaptic cell bodies in the VM thalamus. These cells also have terminals in the left PRL mPFC in the same area (layer 1) receiving input from the LN (Fig. 5f–i). These anatomic connections support previous studies showing functional connectivity between the MN and PRL mPFC12,13,29,35,36.

Posterior vermis function is necessary for normal social and grooming/flexible behaviors, and modulation is sufficient to rescue repetitive behaviors

Considering the connectivity between vermis and mPFC and the association between vermis volume and repetitive behaviors6,33, we hypothesized that the vermis has a role in the regulation of repetitive behaviors. To test this hypothesis, we inhibited posterior vermis PCs in PC^{Cre} mice with DIO-Gi (Fig. 5j and Extended Data Fig. 9). All control groups (VEH-treated or GFP-expressing mice) demonstrated social preferences consistent with the control genotype, whereas chemogenetic inhibition of vermis PCs resulted in impairments in both social approach and social novelty assays (Fig. 5k,l and Extended Data Fig. 9). It also resulted in increased repetitive grooming and behavioral inflexibility in water Y-maze testing

(Fig. 5m,n). Inhibition of posterior vermis PCs did not result in any significant changes in anxiety or locomotion (Extended Data Fig. 9). These results support our hypothesis that the posterior cerebellar vermis regulates social behaviors and behavioral flexibility.

We next asked whether stimulating PC activity in the posterior vermis of PC-*Tsc1* mutant mice is sufficient to ameliorate ASD-relevant behavioral impairments and, specifically, repetitive behaviors. We introduced Cre-dependent stimulation (Gq) or GFP into the posterior vermis of PC-*Tsc1* mutant mice (Fig. 5o). Although chemogenetic stimulation of the posterior vermis did not improve social preference or social novelty preference in the mutant mice (Fig. 5p,q and Extended Data Fig. 9), it reduced repetitive grooming (Fig. 5r) and improved behavioral flexibility in the water Y-maze (Fig. 5s). Stimulation of posterior vermis PCs had no significant effect on locomotion, motor learning or anxiety (Extended Data Fig. 9). These results indicate that posterior vermis PC stimulation selectively rescues repetitive/inflexible behaviors in PC-*Tsc1* mutants. Taken together with its connections to the VM thalamus and VM thalamus inputs to the mPFC (Fig. 5t), these data suggest that cerebellar outputs from Rcrus1 and posterior vermis converge on VM thalamus–mPFC projections to regulate social preference and behavioral flexibility, respectively, and that changes in these cerebellum-thalamus-mPFC pathways might play a role in the impairments in these behavioral domains observed in ASD.

Discussion

One prominent hypothesis is that excitation/inhibition (E/I) imbalance contributes to ASD37. This theory dovetails with findings of elevated cortical activity in individuals with ASD38 as well as synaptic abnormalities resulting in neuronal hyperactivity and altered brain connectivity39. Neural circuit manipulation in combination with neural recordings provide direct evidence that elevated mPFC activity results in ASD-related phenotypes, whereas decreasing mPFC activity is sufficient to rescue abnormal behaviors in ASD models22,23,24. Increasingly, evidence is emerging that decreased inhibition is a critical contributor to E/I imbalance in ASD40. The cerebellum provides an important source of inhibitory tone, as its output emerges solely via inhibitory PCs41. This output is negatively affected in ASD owing to significant PC loss and decreased cerebellar activity2,5,42. In this study, we showed that cerebellar PC dysfunction and targeted inhibition of Rcrus1 or the posterior vermis resulted in increased mPFC activity, consistent with an inhibitory influence of the cerebellum on mPFC activity.

Our data further demonstrate that distinct cerebellar regions regulate specific behaviors, with Rcrus1 stimulation sufficient to ameliorate social behaviors, whereas posterior vermis stimulation is sufficient to improve repetitive/inflexible behaviors. Circuits from these two cerebellar domains and their downstream CN then culminate in VM thalamic circuit regulation of mPFC neurons. Although we demonstrate that cerebellar output connects to the mPFC via these pathways, it is likely that additional cortical, including the clinically implicated right-sided prefrontal cortices20, and other sub-cortical regions might also be regulated by the cerebellum to contribute to ASD-relevant behaviors19. In parallel, other routes might exist by which the cerebellum affects mPFC function, and additional cerebellar targets in the cerebral cortex (Extended Data Fig. 5) might also contribute to these behaviors.

These circuits might include intermediate areas such as the mediodorsal thalamus, the striatum and the ventral tegmental area, especially with recent studies showing that the ventral tegmental area receives direct cerebellar input and that these outputs affect social reward behavior17,43.

Our results further understanding of the roles that the cerebellum plays in the modulation and execution of complex behaviors and support functional connections between the cerebellar cortex and cerebral cortical areas in the regulation of complex non-motor behavior3,9,10,19. Although there is insufficient room to fully discuss the topic here, the mPFC has been demonstrated to have key roles in socio-emotional processing44 and to have critical roles in executive control of behavior. In addition, the cerebellum has been demonstrated to play key roles in making predictions and updating and validating those predictions with real-time sensory information through the use of both implicit and explicit internal forward models (reviewed in ref. 45). These models involve closed-loop interactions between the cortex and cerebellum19. Indeed, from these models, disruption in these delineated circuits that connect the cerebellum and mPFC would be predicted to result in disruption in the ability to generate predictions, validate timing and update those parameters, which, all told, would be expected to have a detrimental effect on social interaction. However, although this study delineates a critical role for these cerebellar-mPFC circuits in the regulation of ASD-relevant behaviors, it will be an important avenue of future research to extend the findings of this study and both uncover the precise function of these regions and circuits during social interactions and further delineate the cerebellar-cerebro cortical network map contributing to these behaviors.

Further delineation of the critical circuit networks would also raise the potential for translational benefit, as neural circuit modulation is a developing avenue for potential therapeutic benefit. However, precise targeting of human mPFC circuits presents a therapeutic challenge owing to the dense processing occurring in the mPFC and because the mPFC offers a less accessible target for noninvasive neuromodulation46. Alternatively, the cerebellum, a more accessible anatomic area, might offer similar, if not greater, therapeutic value for neuropsychiatric disorders47. In fact, stimulation of the cerebellum has been shown to positively alter behaviors while affecting downstream prefrontal cortex function in preclinical studies of schizophrenia48,49. Our findings provide critical insights into how the cerebellum regulates ASD-relevant behaviors, while also offering important preclinical evidence to support a potential cerebellar therapeutic target of neuromodulation through which the therapeutic benefits of mPFC modulation could be leveraged to benefit ASD behaviors. Further understanding of the cerebellar topography and the downstream regulated circuits might thus provide specific therapeutic opportunities for ameliorating disrupted circuitry and behaviors for individuals with neuropsychiatric disorders.

Lastly, these findings demonstrate that social and repetitive behaviors can be improved even in adult mutant mice. Our previous findings have suggested that there is a sensitive period for social behavior that extends into adulthood, whereas the sensitive period for repetitive behaviors closes before adulthood50. However, our current findings that modulation can rescue both social and repetitive behaviors in adulthood suggest that targeted circuit modulation might offer benefit for ASD-related behaviors, even when genetic or

pharmacologically defined sensitive periods are closed. This result raises the possibility that modulatory therapies might even be beneficial for adults with ASD.

Thus, our findings increase mechanistic understanding of the cerebellar-regulated circuit involvement in ASD behaviors and specifically broaden understanding of the diverse brain-wide contributions of the cerebellum to ASD. Moreover, these critical mechanistic insights offer the potential to be leveraged into and contribute to the development of therapeutic avenues for the treatment of ASD.

Methods

For more details, see the Nature Research Reporting Summary.

Mice

L7/Pcp2-Cre (*L7*^{Cre}) transgenic mice51 were obtained from Jackson Laboratories. *PC*^{Cre};*Tsc1*$^{flox/flox}$ (PC-*Tsc1* mutant) animals were generated by crossing *L7/Pcp2-Cre* (*PC*^{Cre}) transgenic mice with floxed *Tsc1* mice (*Tsc1*$^{flox/flox}$)52 to yield *PC*^{Cre};*Tsc1* $^{flox/+}$ progeny. These progeny were then crossed with one another to ultimately yield *Tsc1*$^{flox/flox}$ and *PC*^{Cre};*Tsc1*$^{flox/flox}$ mice. These were then used as breeders with *Tsc1*$^{flox/flox}$ mice crossed to *PC*^{Cre};*Tsc1*$^{flox/flox}$ mice. Only male animals were used for behavioral experiments and electrophysiological recordings. Mice were aged 5–12 weeks. Mice were of mixed genetic backgrounds (C57Bl/6J, 129 SvJae and BALB/cJ). Littermate controls were used for all behavioral experiments. Ai14 Td tomato reporter mice were used with AAV-1^{Cre} injections for tracing experiments53. The University of Texas Southwestern and John Hopkins University Institutional Animal Care and Use Committees approved all experimental protocols in this study.

Stereotaxic viral injections and optical fiber implantation

Viral vectors used in behavioral experiments were delivered to the prefrontal cortex and cerebellum with a nanoinjector (WPI) under stereotaxic guidance (Stoelting) in ketamine anesthetized mice. AAV1.hSyn.Cre.WPRE.hGH, AAV9.hSyn.eGFP.WPRE.bGH, AAV9.hSyn.TurboRFP.WPRE.rBG, cholera toxin B (CTB)-488, AAV5-hSyn-mCherry, AAV8-hSyn-DIO-hM3D(Gq)-mCherry (hM3Dq), AAV8-hSyn-DIO-hM4D(Gi)-mCherry (hM4Di), AAV8-CMV-GFP, AAV2-hSyn-hM3D(Gq)-mCherry and AAV2-hSyn-hM4D(Gi)-mCherry, AAV8-CamKIIa-hM3D(Gq)-mCherry or optogenetic constructs (ChR2 (AAV5-hSyn-hChR2(H134R)-mCherry) and Arch 3.0 (AAV5-hSyn-eArch3.0-EYFP)) were used for viral injections. Injection volumes varied depending on virus usage (3–50 nl for tracing experiments and 100–350 nl for behavioral experiments and recordings depending on the size of the brain areas injected). All viruses were purchased from the UNC Viral Vector Core or Addgene. All viral titers were 10^{12} vg ml^{-1}. Location of injections were as follows (*x, y, z*): left PRL mPFC: −0.5, 2.10, −2.0; left VM thalamus: −0.7, −0.8, 4.0–4.2; right LN: −2.0, −6.24, −3.5; Rcrus1: −2.5, −6.36, −2.5; vermis VII/VIII: midline, −4.75 from lambda, −1.0. For optogenetic experiments, 1-mm optical fibers were implanted into the left PRL mPFC and secured with Krazy Glue and dental cement.

In vivo awake recordings

Subjects were surgically implanted with custom-made microdrive arrays (8–10 g) designed to target the specific and relevant regions outlined in the study. Briefly, design of microdrive arrays was facilitated using Solidworks software with fabrication of core components (microdrive body, custom cannula and protective covering) achieved using a 3D printer (Formlabs). Each microdrive array contained independently adjustable, gold-plated tetrodes targeting the PRL (*x*, *y*, *z*: −0.5, 2.10, −2.0). Each tetrode consisted of a twisted bundle of four 17.8-mm platinum/10% iridium wires. Each wire was electroplated with gold to an impedance of <150 MΩ before surgery. Small jewelry screws (Component Supply) were used to anchor microdrives to the skull of the animal. One anchor screw served as a ground. Tetrodes were lowered to hypothetical recording depths during implantation surgery, and depths were not adjusted during/after the surgery at any point unless otherwise noted. Subjects were implanted under regulated isoflurane anesthesia; postoperative analgesic was administered subcutaneously in the form of buprenorphine (0.006 mg ml^{-1} at 0.01 ml g^{-1} body weight). Exposure to experimental arenas and behavioral paradigms occurred after animals had fully recovered from implantation surgery and accustomed to the weight of implanted microdrive arrays. All implanted animals had access to chow and water ad libitum in their home cages throughout experiments unless described otherwise.

All data were collected using a Neuralynx data acquisition system and an overhead video system that recorded continuously at 30 Hz. Animal position and head direction were determined via infrared tracking stickers at rostral and caudal extremes of each microdrive. Analog neural signals were digitized at 32,556 Hz. Spike threshold crossings (50 μV) were recorded at 32,556 Hz. Continuous local field potential data were digitally filtered between 0.1 and 500 Hz and recorded at 3,255.6 Hz. Recording locations were verified post hoc via electrolytic lesions and histologic analysis of 50-μm coronal sections.

Tracing experiments

Stereotaxic tracer injections were made into adult B6 mice or Ai14 mice in case of AAV-mediated anterograde trans-synaptic tracing28.

AAV9.hSyn.TurboRFP.WPRE.rBG and AAV9.hSyn.eGFP.WPRE.bGH were used for anterograde axonal tracing, and AAV1.hSyn.Cre.WPRE.hGH was used for anterograde trans-synaptic tracing. Additionally, CTB-448 was used in combination with AAV-1 anterograde tracing for supplemental tracing experiments.

Mice were placed on the stereotaxic apparatus under ketamine or isoflurane anesthesia (2% in 1.0 L min^{-1} oxygen). A small incision was made in the head skin of the mouse, and a small hole was drilled in the skull. A pulled glass pipette (tip inner diameter, 5–15 μm) filled with a tracer was stereotaxically inserted in the brain using an Angle One stereotaxic instrument (myNeuroLab.com), and a small amount of the tracer (3–50 nl) was pressure injected using Picospritzer II (Parker Hannifin) with nitrogen (15–30 psi) at the target. To more precisely localize tracer injections to the LN/MN, cerebellar local field potentials were monitored with an extracellular amplifier (ER-1, Cygnus; bandpass frequency 1–3,000 Hz), a 50/60-Hz noise eliminator (HumBug, Quest Scientific) and a speaker. Ten minutes after

the injection, the glass pipette was removed from the brain and the skin was sutured. After surgery, we waited 3 weeks for AAV axonal transport, 4 weeks for AAV trans-synaptic somatic labeling and 5 weeks for AAV trans-synaptic axonal transport. After appropriate transport periods, mice were deeply anesthetized with 2,2,2-tribromoethanol (also known as avertin, 0.5 mg g^{-1}) and then were transcardially perfused with phosphate-buffered saline (PBS) containing heparin (10 U ml^{-1}) followed by 4% paraformaldehyde (PFA) in PBS. Brains were dissected out from the skull, post-fixed overnight in 4% PFA in PBS and cryoprotected in 30% sucrose PBS. The brains were embedded in gelatin to prevent separation of the cerebellum from the brainstem. The gelatin blocks were hardened on ice and then trimmed and fixed overnight with 4% PFA in 30% sucrose PFA. Coronal serial sections were cut at a thickness of 40 μm with freezing microtome. After being rinsed with PBS, the sections were stored in PBS containing 0.1% sodium azide at 4°C until use. The sections were rinsed with PBS, mounted on slide glass and coverslipped with VECTASHIELD (H-1400, Vector Laboratories).

Anatomical data analysis—We used the Paxinos mouse brain atlas54 for anatomical nomenclature. When needed, we also used other nomenclature based on literature. Images were taken with a confocal microscope system (FV1000, Olympus) or a charped-coupled device camera (ORCA-100, Hamamatsu) attached with an epi-fluorescent microscope (BX61, Olympus). Contrast and brightness were adjusted in Photoshop CS6 (Adobe). In some panels, low-magnification images were made by tiling several photos of higher magnification. For mapping disynaptic input to the cortex, we used a functional cortical map55 with modification.

Chemogenetic and optogenetic activation

CNO was purchased from Tocris Bioscience and reconstituted to 1 mg ml^{-1} concentration with 0.9% saline with dimethyl sulfoxide to 0.5%56. VEH contained 0.9% saline with DMSO to 0.5%. Mice were injected intraperitoneally with 2 mg kg^{-1} CNO 30 min before behavioral testing. For in vivo recordings, mice were injected with 2 mg kg^{-1} CNO after 10 min of baseline recording.

Doric Connectorized Laser Diode Module 473 nm and Module 520 nm (CLDM_473/070 and CLDM_520/060) were used with a transistor–transistor logic pulse generator (OTPG_4). ChR2 was activated with either 20-Hz continual or 4-Hz 5-ms blue light pulses during behavioral testing. Arch 3.0 was activated with green light at 20-Hz continual or 4-Hz 5-ms pulses during behavioral testing. Laser output varied between 5- and 10-mW output from optical fibers that were tested before implantation.

Electrophysiology in acute slices

Acute slice recordings were performed as described previously5. In brief, after allowing 1–3 weeks for ChR2 or Arch expression, two or three acute horizontal thalamus brain slices were prepared from 4–8-week-old mice for in vitro recording and stimulation (300-μm thick). Slices were cut in an ice-cold artificial cerebrospinal fluid (ACSF) solution consisting of (in mM) 125 NaCl, 26 $NaHCO_3$, 1.25 NaH_2PO_4, 2.5 KCl, 1 $MgCl^2$, 2 $CaCl_2$ and 25 glucose (pH, 7.3; osmolality, 310) equilibrated with 95% O_2 and 5% CO_2. Slices were initially

incubated at 32 °C for 30 min and then at room temperature for 45 min before recording in the same ACSF. Visually guided (infrared differential interference contrast video microscopy and water immersion ×40 objective) whole-cell recordings were obtained with patch pipettes (4–6 MΩ) pulled from borosilicate capillary glass (World Precision Instruments) with a Sutter P-1000 horizontal puller. Electrophysiological recordings were performed in the recording chamber at 32 °C. Thalamus neurons in brain slices were visualized by microscopy with UV.

The internal solution contained (in mM) 150 K-gluconate, 3 KCl, 10 HEPES, 0.5 EGTA, 3 MgATP, 0.5 GTP, 5 phosphocreatine-tris2 and 5 phosphocreatine-Na2. pH was adjusted to 7.2 with NaOH. Experiments were conducted with Axon Instruments hardware and software (Multiclamp 700B, Digidata 1440A and pClamp 10).

For optical stimulation, to assess responses to optical stimulation of thalamus neurons with ChR2 or Arch expressed, we used a blue laser at wavelengths of 440–470 nm and a green laser at wavelengths of 570–590 nm during recording by current clamp.

Miniature EPSCs were recorded at −70 mV in ACSF containing 1 μM tetrodotoxin (TTX) and picrotoxin (20 μM), whereas miniature IPSCs were recorded at +10 mV in the presence of 1 μM TTX, 5 μM (RS)-CPP 5 μM and 2,3-dioxo-6-nitro-1,2,3,4-tetrahydrobenzo[f]quinoxaline-7-sulfonamide. The internal pipette solution contained (in mM) 140 Cs-methanesulfonate, 15 HEPES, 0.5 EGTA, 2 TEA-Cl, 2 MgATP, 0.3 NaGTP, 10 phosphocreatine-tris2 and 2 QX 314-Cl. pH was adjusted to 7.2 with CsOH. Recordings were included only when a GΩ seal formed before whole-cell access. Whole-cell patch-clamp recordings were obtained from pyramidal cells in layers 2/3 of the PRL cortex. Pyramidal neurons were distinguished from interneurons by their shape, spiking pattern and action potential. In addition, their identity was confirmed by their large apical dendrites, which were visualized by using Neurobiotin staining.

Mouse in vivo electrophysiology

Male and female mice were used for in vivo anesthetized extracellular single-unit recordings. Recordings were done as described previously8. In brief, mice were anesthetized using a combination of ketamine (100 mg kg^{-1}) and xylazine (10 mg kg^{-1}) and placed in a stereotaxic apparatus, and a TC-1000 temperature controller with rectal probe was used to keep the mice at 37 °C. Craniotomies were performed to remove a rectangular patch of skull over each recorded brain area. Care was taken to avoid surface blood vessels during microelectrode insertion, and dura was kept intact and moistened with saline during the experiment. Tungsten microelectrodes (World Precision Instruments; 3-μm insulation, 0.356-mm shaft, 2 MΩ, 1–2-μm tip) were inserted to each desired depth (same stereotaxic locations as viral injections), and electrophysiological activity was acquired, amplified and band-pass filtered (low-pass filter, 5 kHz; high-pass filter, 300 Hz) with a MultiClamp 700B programmable amplifier (Molecular Devices). For experiments with CNO modulation, CNO was administered after acquiring 10 min of baseline recording. Average frequency after CNO was calculated by averaging frequency of single units from 60–70 min and normalizing to baseline frequency. All raw values for frequency of spiking (shown in figures as normalized values) can be found in Extended Data Fig. 10. Recordings with optogenetics

were analyzed by collecting 10-min baseline single-unit frequency and average frequency during 10 min with laser stimulation (4 Hz in 5-ms pulses or 20 Hz continuous). Mice were randomly assigned to treatment groups. Data analysis was done offline using codes written in MATLAB, and Wave_Clus was used for semi-automated spike sorting and clustering of single units.

Mouse MRI

Animal preparation—Experimentation complied with all ethical regulations. The animal care protocol was approved by the Toronto Centre for Phenogenomics as well as the institutions that provided the mice. Given that the MRI scanning, registration and volume measurements were an automated process, the experimenters were not blinded to genotype.

Anesthesia was performed in the mice using a mixture of ketamine and xylazine. The mixture was intracardially perfused with 30 ml of 0.1 M PBS with 10 U ml^{-1} heparin (Sigma) and 2 mM of our gadolinium contrast agent, ProHance, followed by 30 ml of 4% PFA containing 2 mM ProHance. Mice were decapitated after perfusion. The skin, lower jaw, ears and nose were removed as previously described. The brain remained within the skull, and both were incubated overnight in 4% PFA containing 2 mM ProHance at 4 °C. The brain and skull were then transferred to 0.1 M PBS containing 2 mM ProHance and 0.02% sodium azide for at least 1 month before MRI scanning[57,58].

Our full data set consisted of 94 genotypic models of ASD (2,414 mice, 67.7% male, PND 30–245) (Supplementary Table 3). When this data set was analyzed, significant differences (FDR corrected $q < 0.05$) in covariance were observed between Rcrus1 and the left PRL mPFC in addition to posterior vermis and this region. To examine whether certain subsets of models might be contributing to this effect, significant volume differences per genotype were identified within both the left mPFC and cerebellar regions of interest (ie, Rcrus1 and posterior vermis) separately for each model. Thirty models with $P < 0.05$ in both the left mPFC and the cerebellar regions were identified, and structural covariance analysis on these models ($n = 559$) and controls ($n = 1,101$) was also performed (demographics included in Supplementary Table 3). For each mouse line, the control mice were prepared and provided by the same facility that provided the mutant mice, with some facilities providing multiple mutations.

MRI sequence details—A 7T MRI scanner (Agilent) was used to acquire all images. Images were acquired between 2012 and 2017. In this time, the scan protocol was modified to increase throughput and resolution while maintaining consistent signal-to-noise ratio and tissue contrast. All mice were scanned using a T2-weighted fast spin echo sequence, with three different sets of parameters. Most mice were scanned using Sequence 3. Either an insert gradient with an inner bore diameter of 6 cm or an outer gradient with a 30-cm inner bore diameter was used, as previously described[59,60,61].

Sequence 1 was used to scan three brains per overnight session. Three custom-built solenoid coils were used for parallel imaging[58,59]. The parameters—optimized for high contrast between white and gray matter—were as follows: repetition time (TR) = 325 ms, echo time (TE) = 10 ms per echo for six echoes (the center of k-space was acquired on echo 4), four

averages, field of view (FOV) = 14 × 14 × 25 mm^3, a matrix size of 432 × 432 × 780 and 32-μm isotropic voxels. Total imaging time was approximately 12 h57,62,63.

Sequence 2 was used to scan 16 brains per overnight session, using an in-house custom-built 16-coil solenoid array to acquire images in parallel57,62,63. The parameters were as follows: TR = 2,000 ms, TE = 42 ms per echo for six echoes, FOV = 25 mm × 28 mm × 14 mm, a matrix size of 450 × 504 × 250 and 56-μm isotropic voxels. Alternating echoes were used to acquire consecutive k-space lines. This was done to move ghosting artifacts to the periphery of the FOV60,61,64. The phase-encoding direction was oversampled by a factor of 2 to avoid interference from these artifacts. This direction was then cropped to 14 mm after reconstruction. Total imaging time was approximately 12 h.

Sequence 3 was used to scan 16 brains per overnight session, using the 16-coil solenoid array used for Sequence 258,62,63. k-space was acquired using a cylindrical acquisition65. The parameters were as follows: TR = 350 ms, TE = 12 ms per echo for six echoes, FOV = 20 × 20 × 25 mm^3, a matrix size of 504 × 504 × 630 and 40-μm isotropic voxels. Total imaging time was approximately 14 h.

Statistical analysis

All statistical analyses were performed using the R statistical package (https://www.r-project.org/). Brain volumes were segmented according to the publicly available Dorr–Steadman–Ullman–Richards–Qiu–Egan 40-μm atlas, which defines 180 structures (356 bilaterally) within a three-dimensional atlas of adult C57Bl/6J mice66,67,68,69. Segmentation and labeling were performed using the RMINC package (https://github.com/Mouse-Imaging-Centre/RMINC). All regional volumes were normalized to total brain volume for each mouse before model fitting. A linear regression model with interaction-with-genotype and interaction-with-sex terms was fit to brain volume data to compare pairs of structures. Sex and interaction with sex were included as covariates in the structural covariance model used to measure the interaction-with-genotype effect. In this model, ‘genotype’ is a two-level factor, with ‘wild type’ and ‘mutant’ as the two levels. The interaction-with-genotype coefficients were tested for significance using a two-sided *t*-test. *P* values were corrected for multiple comparisons using the Benjamini–Hochberg procedure; these FDR-corrected *P* values are herein referred to as *q* values. The coefficient of determination (R^2) for each model was also evaluated.

Human structural MRI

The human brain imaging data come from the POND network as well as data collected in a series of experiments in the lab of M.J.T. These studies were approved by the Hospital for Sick Children’s Research Ethics Board. All scans were acquired on the same 3T Siemens magnet, although there was an upgrade between the Tim Trio and the Prisma in between. A total of 1,222 scans from 786 individuals were processed. T1 scans (Trio: TR/TE 2,300/2.96 ms, flip angle (FA) 9°, FOV 192 × 240 × 256 mm, 1.0-mm isotropic voxels, scan time 5 min; Prisma: TR/TE 1,870/3.14 ms, FA 9°, FOV 192 × 240 × 256 mm, 0.8-mm isotropic voxels) were processed. Cerebellar volumes were segmented using the MAGeT pipeline70,71. Cortical volumes were extracted from the CIVET v2.1 pipeline72,73,74.

After quality control, 902 scans (425 ASD and 477 control) from 648 individuals (285 ASD and 368 control) were considered for analysis. Age range was 2–50 years, with a mean age of 13 years.

We tested whether covariance between cerebellar and cortical regions differed by diagnosis. First, we used Rcrus1 as our seed and six separate left hemisphere cortical regions as targets (mPFC, medial orbitofrontal anterior cingulate cortex, anterior cingulate/paracingulate, gyrus rectus, superior frontal gyrus (medial orbital part) and superior parietal gyrus). Next, we removed overall brain volume by dividing each region by total brain volume. Volumes were then standardized by subtracting the mean and dividing by the s.d. A regression model then tested for the seed region against the target region, diagnosis, diagnosis and target interaction, covariates for scanner (Prisma or Trio), age at scan and sex. If an individual had more than one scan, the volumes were averaged (multiple scans were acquired in the same session or within a short period of time of each other). The diagnosis by target interaction was of primary interest. To ensure that our brain volume covarying strategy did not unduly influence the results, we repeated the analyses using log regressions as in ref. 75. The results were largely identical.

Human functional MRI

The study was approved by the American University Institutional Review Board. Eight TD male adults (mean age, 20.75 ± 1.91 years) and eight male adults with ASD (mean age, 26.13 ± 9.79 years) provided written, informed consent to participate in the study. Functional MRI was performed on Georgetown University's Center for Functional and Molecular Imaging's Magnetom Trio 3T scanner with a 12-channel head coil. Resting state data were acquired as part of a larger study (results to be reported elsewhere). Participants underwent a 5-min, 50-s resting state scan, during which they rested comfortably with their eyes open (acquisition parameters: TR = 2.5 s, TE = 30 ms, 47 interleaved slices, 3.2-mm slice thickness, 3.2-mm voxel size, 90° FA, 140 volumes (this does not include dummies)). Participants also completed a high-resolution T1 MP-RAGE structural scan (acquisition parameters: TR = 1.9 s, TE = 2.52 ms, 176 interleaved slices, 1.0-mm slice thickness, 0.98-mm voxel size, 9° FA).

Data analyses were performed using the CONN toolbox (version 18b; www.nitrc.org/projects/conn, RRID:SCR_009550) implemented in MATLAB (version R2018b). Group MVPA was conducted using CONN with three factors and a dimensionality reduction of 64. Voxel-to-voxel functional connectivity maps thresholded at $P < 0.001$, FDR cluster corrected $P < 0.05$ yielded significant clusters in the medial prefrontal cortex (peak coordinates (*x, y, z*): 4, 38, −24; k = 260) and Rcrus 1 and Rcrus2 of the cerebellum (peak coordinates (*x, y, z*): 34, −82, −40; k = 18). Seed-to-voxel post hoc analyses were then performed from these seeds to examine whether there were group differences in functional connectivity between the medial PFC and the Rcrus1 Rcrus2 cerebellar clusters. Seeds were created by extracting the medial prefrontal and cerebellar clusters, and seed-to-voxel results comparing functional connectivity in the ASD and TD groups were thresholded at $P < 0.001$, FDR cluster corrected $P < 0.05$.

Behavioral analysis

Statistics of behavioral experiments can be found in Supplementary Tables 1 and 2. Behavioral studies were performed with male mice, with repeat testing performed for the following behavioral tests: elevated plus maze, open field, three-chambered apparatus, grooming and olfaction testing. Mice were randomly assigned to groups for viral injection type. Each mouse performed these testing paradigms with VEH and CNO. Starting treatment was randomly assigned and then alternated between VEH and CNO treatments. To minimize previous exposure to the task, repeated testing in a specific behavioral paradigm was separated by 1 week. Testing was performed in the order listed above. For rotarod and water maze testing, which were performed in the weeks after the above testing, mice were randomly assigned to one treatment group (either VEH or CNO), and no repeat testing was performed owing to the learning component involved in these tests. Animals were group housed under a 12-h light:dark cycle. Chemogenetic studies involved the following controls: GFP infection (VEH and CNO) and designer receptors exclusively activated by designer drugs (DREADD) infection (VEH and CNO) for all behavioral studies to control for DREADD activation and potential effects of VEH and to control for CNO off-target effects76. Optogenetic studies involved the following controls: GFP infection (light ON and OFF) and ChR2/Arch infection (light ON and OFF) to control for optogenetic stimulation/inhibition and potential effects of light versus surgical procedure77. All behavioral assays were performed by examiners blinded to genotype.

Open field—Open field testing was conducted at 6–10 weeks of age in a 17.5-inch square box for 15 min as previously described78. Distance traveled in the open field and time spent in the center quadrant were quantified by Noldus EthoVision tracking. Center zone was marked as a 14-cm square. Light was kept at 40 lux and tested at the center of the open field.

Elevated plus maze—Elevated plus maze testing was conducted between 6 and 10 weeks of age as previously described. Briefly, testing was conducted for 5 min with time in the open arm and total distance traveled calculated with EthoVision tracking. Light in the open arms was kept at 30 lux.

Accelerating rotarod—Animals were tested using the accelerating rotarod as previously described over 5 consecutive days79. Latency to fall was recorded.

Three-chambered social testing—Male mice between 7 and 11 weeks old were tested with the three-chambered social approach and social novelty assays as described previously80. Time in each chamber was calculated through automated tracking, and time spent sniffing was calculated by examiner and by automated detection (TopScan, CleverSys and Noldus EthoVision). Briefly, the three-chambered apparatus (Nationwide Plastics) was in a room with 30-lux lighting at the center of the apparatus and a celling-mounted camera for EthoVision tracking. The mice were socially isolated for 30 min before testing and then habituated to the center chamber for 10 min. Then, recording was started, and the mice were allowed to explore all three chambers for another 10-min habituation period. For social approach testing, an empty wire cup and a wire cup with an age- and gender- matched C57 mouse were added in opposite side chambers, and the mouse was tested for 10 min. Then,

another C57 mouse was added to the previously empty cup for another 10 min of testing for social novelty.

Grooming—Male mice, 6–11 weeks old, were habituated to an empty cage for 10 min and then timed for self-grooming behavior for 10 min81. Mice were tested in red light between 18:00 and 22:00. Grooming time was recorded by an examiner with a stopwatch.

Social olfaction—Olfaction was tested in 8–11-week-old mice as described previously82. Mice were exposed to each scent in three consecutive 2-min trials in the following order: water, almond (Kirkland), banana (imitation, McCormick), social 1 and social 2. Social scents were collected from the dirty cages of age- and gender-matched unfamiliar mice. Time spent sniffing was recorded with a stopwatch by an examiner.

Water T-maze/water Y-maze—Reversal learning in the water T-maze or water Y-maze was conducted as described previously83. Mice 8–12 weeks of age were tested with 3 d of 15 trials per day to locate a submerged platform in one arm of the maze. For the following 3 d, the platform was moved to the opposite arm, and the mice were tested for finding the new platform location. Number of correct trials out of 15 was calculated for each day.

Statistics

Behavioral data are reported with box and whisker plots. Medians are denoted by the box lines with 5–95% denoted by the whiskers.

Electrophysiological recordings are shown as mean ± s.e.m., and statistical analysis was carried out with GraphPad Prism software. Two- or three-way ANOVAs with post hoc Sidak's multiple comparison tests were used to evaluate significance for behavioral tests. Outlier tests were also conducted using the robust regression outlier test in the Prism software suite to determine if data should be excluded. Six datum were found to be outliers across all mini EPSC/IPSC recordings and were excluded.

Electrophysiological data were analyzed with Prism software and tested for normality of distribution with a one-tailed Kolmogorov–Smirnov test. If data were found to be normal, a two-tailed Student's *t*-test was used. If data were found not to be normally distributed, a Mann–Whitney test was used to test for significance between groups. For all other data, data distribution was assumed to be normal, but this was not formally tested. The sample size estimate was performed based on a repeated-measures ANOVA design (mixed-model ANOVA with covariance structure of compound symmetry) using PASS 12 to estimate sample size5,8.

Reporting Summary

Further information on research design is available in the Nature Research Reporting Summary linked to this article.

Extended Data

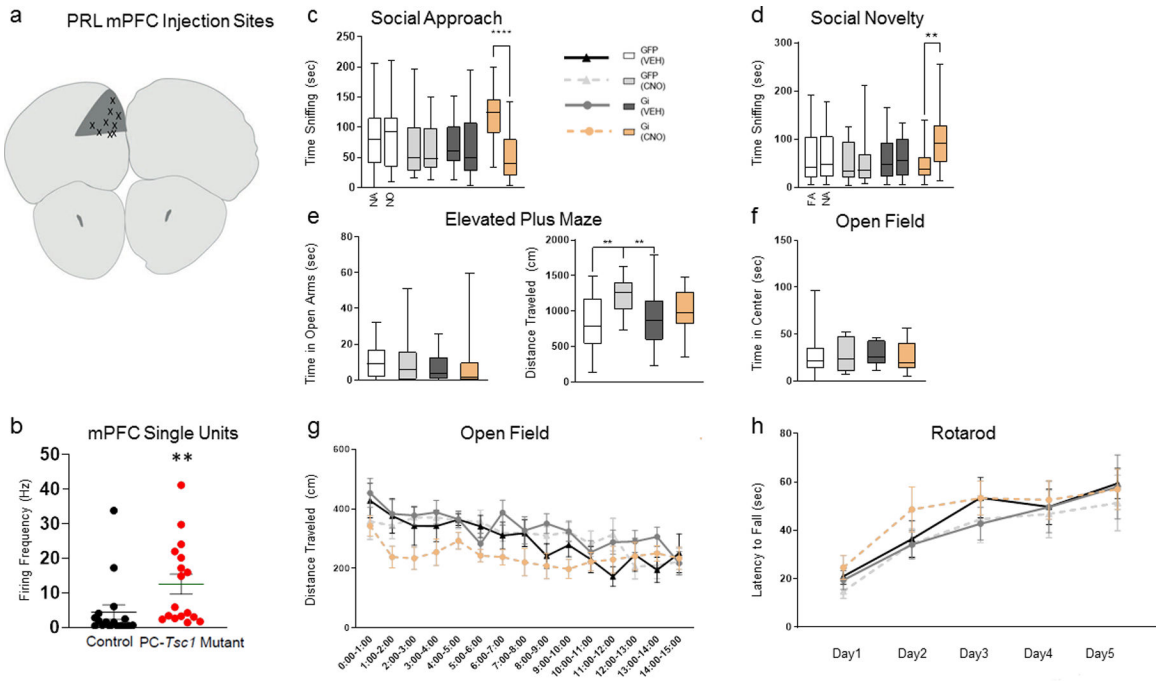

Extended Data Fig. 1. mPFC Gi DREADDs in PC-Tsc1 mutant mice.

a, Sample of injection site locations from PC-*Tsc1* mutants injected with Gi (inhibitory) DREADDs/GFP into left prelimbic (PRL) medial prefrontal cortex (mPFC). **b**, Awake *in vivo* single unit recordings in the left PRL of control or PC-*Tsc1* mutant mice. **c**, Three chambered social approach assay; time spent sniffing novel animal (NA), or novel object (NO). **d**, Three chambered social novelty testing; time spent sniffing NA or familiar animal (FA). **e**, Time in the open arm and distance traveled in the elevated plus maze assay. **f**, Time in the center of the open field and **g**, distance traveled in the open field. **h**, Latency to fall in accelerating rotarod test. Box line denoted median/whiskers denoted 5–95%. n ≥ 10 for all experiments. All behavioral tests were analyzed with two or three-way ANOVA and Sidak post test and single unit recordings were analyzed with Mann-Whitney test, shown as mean SEM. ****$P < 0.0001$; ***$P < 0.001$; **$P < 0.01$; *$P < 0.05$. P values and complete animal numbers can be found in Supplementary Table 2.

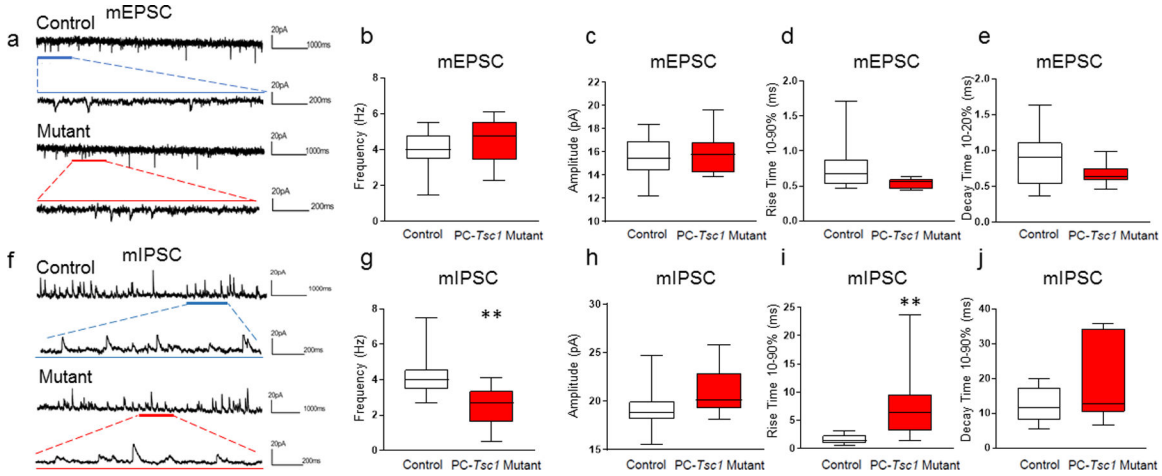

Extended Data Fig. 2. Left Prelimbic Synaptic Properties in PC- Tsc1 Mutant Mice.

a, mini EPSC (mEPSC) representative traces with zoomed in views below initial traces as noted; **b**, mEPSC frequency; **c**, mEPSC amplitude; **d**, mEPSC rise time; **e**, mEPSC decay time; **f**, representative mIPSC traces with zoomed in views blow initial traces as noted; **g**, mIPSC frequency; **h**, mIPSC amplitude; **i**, mIPSC rise time; **j**, and mIPSC decay time in PC-*Tsc1* mutant mice and control mice. Groups had 12–15 cells from 5 animals in each. Students t-test, ****$P < 0.0001$; ***$P < 0.001$; **$P < 0.01$; *$P < 0.05$.

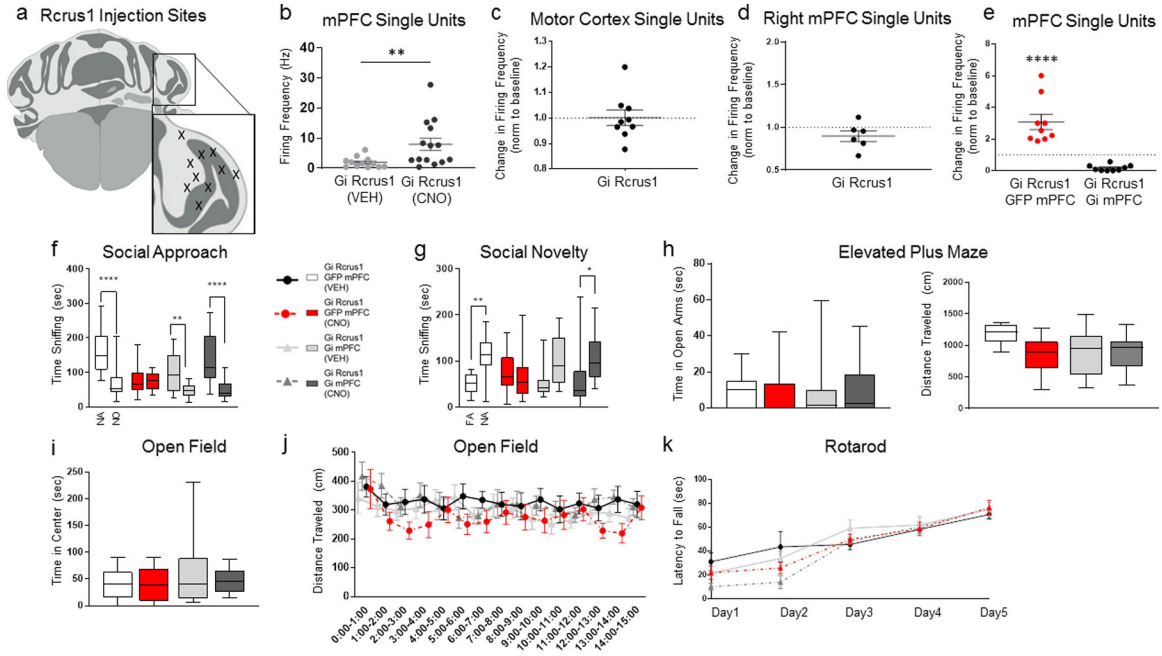

Extended Data Fig. 3. Impact of chemogenetic inhibition of mPFC on Rcrus1 PC inhibition-regulated behaviors.

a, Sample injection site locations in area Rcrus1. **b**, Awake *in vivo* single unit recordings in prelimbic cortex (PRL) in mice with Rcrus1 Gi DREADD inhibition (CNO) or vehicle treatment. **c**, *In vivo* single unit recordings in motor cortex of anesthetized mice with Rcrus1 Gi DREADDs inhibition compared to baseline. No significant change identified. **d**, *In vivo*

single unit recordings in right PRL of anesthetized mice with Rcrus1 Gi DREADD inhibition compared to baseline. No significant change identified. **e**, *In vivo* single unit recordings in left PRL of anesthetized mice with Rcrus1 Gi DREADD inhibition and either GFP or Gi injection in the mPFC. **f**, Three chambered social approach assay; time spent sniffing novel animal (NA), or novel object (NO). **g**, Three chambered social novelty testing; time spent sniffing NA, or familiar animal (FA). **h**, Time in the open arm and distance traveled in the elevated plus maze assay. **i**, Time in the center of the open field and **j**, distance traveled in the open field. **k**, Latency to fall in accelerating rotarod test. All behavioral tests were analyzed with two or three-way ANOVA and Sidak post test. Single unit recordings were analyzed with Mann-Whitney test, shown as mean SEM. All raw values for frequency of spiking that are shown in figures as normalized values can be found in Extended Data Fig. 10. Box line denoted median/whiskers denoted 5– 95%. n ≥ 10 for all behavioral experiments. ****$P < 0.0001$; ***$P < 0.001$; **$P < 0.01$; *$P < 0.05$. P values and complete animal numbers can be found in Supplementary Table 2.

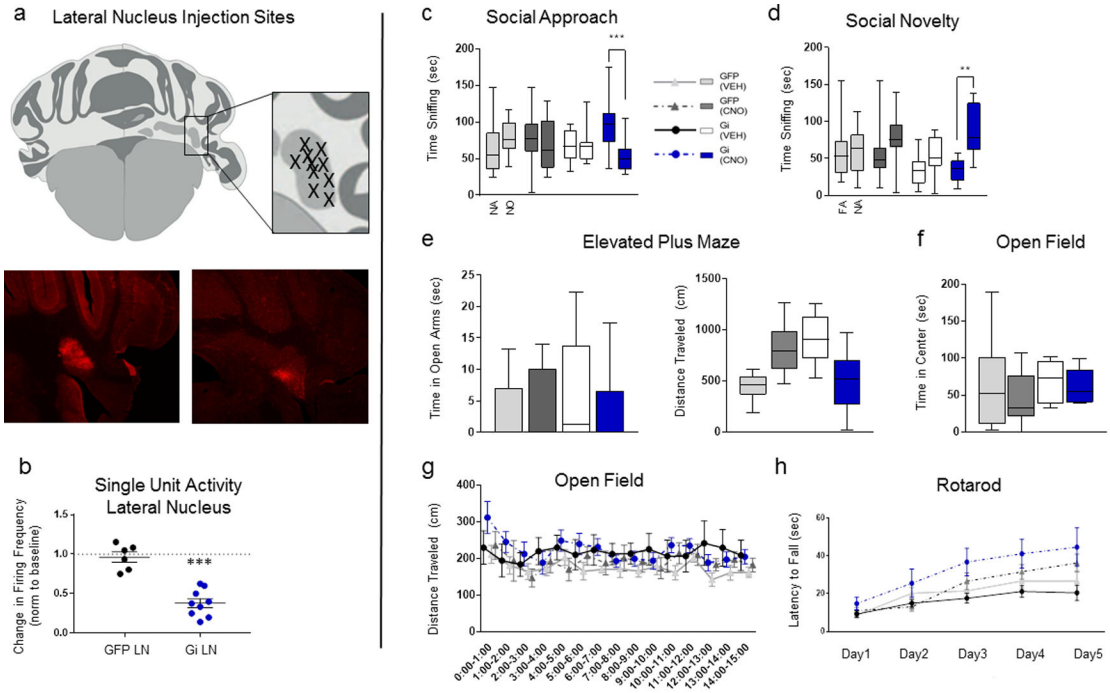

Extended Data Fig. 4. Inhibition of LN in PC-Tsc1 mutant mice.

a, Sample injection site locations and injection site pictures of Gi DREADDs injected into LN of PC-*Tsc1* mutant mice. **b**, Single unit activity in the right lateral nucleus (LN) with chemogenetic inhibition (Gi) or control GFP injection. **c**, Three chambered social approach assay; time spent sniffing novel animal (NA), or novel object (NO). **d**, Three chambered social novelty testing; time spent sniffing NA, or familiar animal (FA). **e**, Time in the open arm and distance traveled in the elevated plus maze assay. **f**, Time in the center of the open field and **g**, distance traveled in the open field. **h**, Latency to fall in accelerating rotarod test. All behavioral tests were analyzed with two or three-way ANOVA and Sidak post hoc testing. Recordings were analyzed with Mann-Whitney test, shown as mean SEM. For frequency of spiking shown in figures as normalized values, raw values can be found in

Extended Data Fig. 10. Box line denoted median/whiskers denoted 5–95%. n ≥ 10 for all behavioral experiments. ****$P < 0.0001$; ***$P < 0.001$; **$P < 0.01$; *$P < 0.05$. P values and complete animal numbers can be found in Supplementary Table 2.

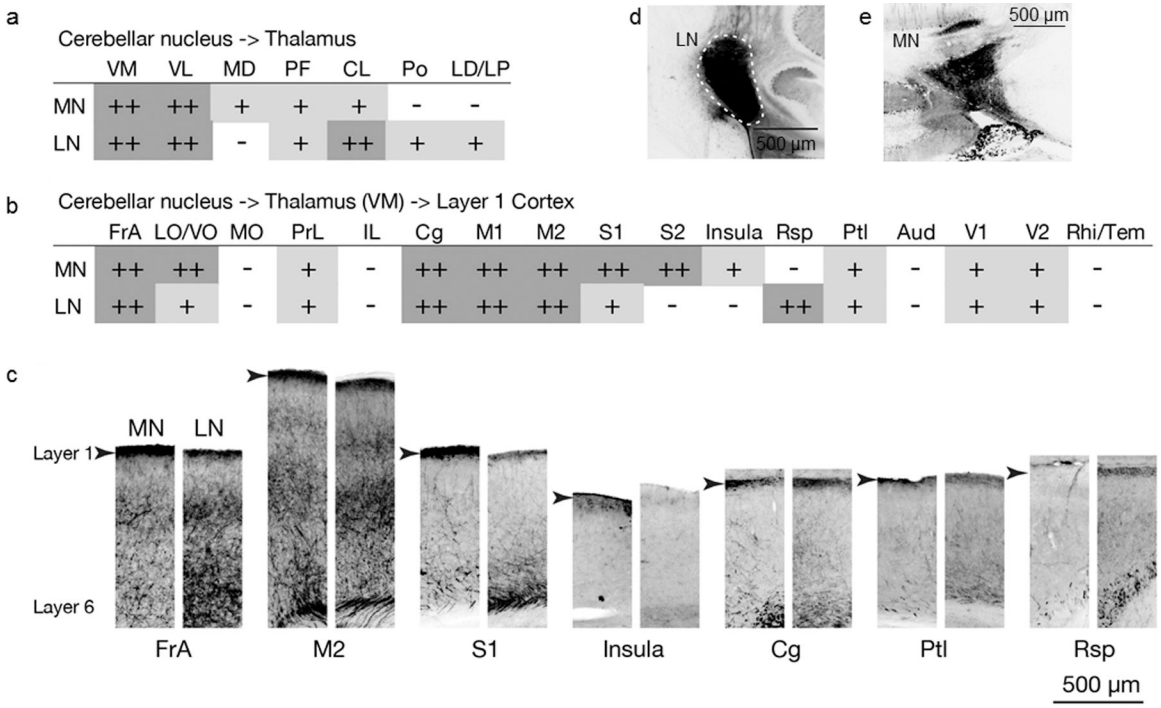

Extended Data Fig. 5. Thalamic and layer 1 cortical areas targeted by the medial and lateral cerebellar nuclei.

a, Thalamic nuclei with monosynaptic inputs from the right medial nucleus (MN) and lateral nucleus (LN) identified via AAV1-mediated anterograde transsynaptic tracing. The number of the trans-synaptically labeled thalamic neurons in each nucleus indicated as + + (high), + (low), and - (none). **b**, Disynaptic inputs from the right MN and LN to distinct cortical regions of the left cerebral cortex, identified via transsynaptic tracing. Labeled input density to layer 1 of each cortical area is indicated as + + (high), + (low), and - (none). **c**, Representative tracing results of disynaptic inputs from the right MN and LN to distinct areas in the left cerebral cortex. Axons and terminals of thalamic neurons trans-synaptically labeled from injections to MN and LN are indicated in black. Results from injections to MN and LN are in the left and right, respectively, of each panel. Top and bottom parts of each panel correspond to layer 1 and 6. Inputs to layer 1 originate predominantly from the VM thalamus. Arrowheads indicate layer 1. Scale bar applies to all panels. **d**, representative injection site in the LN and **e**, representative injection site in the MN. Scale bar applies to all panels. Abbreviations; Aud, auditory cortex; Cg, cingulate cortex; CL, centrolateral thalamic nucleus; FrA, frontal association cortex; IL, infralimbic cortex; LD, laterodorsal thalamic nucleus; LO, lateral orbital cortex; LP, lateroposterior thalamic nucleus; M1 and M2, primary and secondary motor cortex; MD, mediodorsal thalamic nucleus; MO, medial orbital cortex; PF, parafascicular thalamic nucleus; Po, posterior thalamic group; PrL, prelimbic cortex; Ptl, parietal association cortex; Rhi, ecto-/peri-/ento-entorhinal cortex; Rsp, retrosplenial cortex; S1 and S2, primary and secondary sensory cortex; Tem, temporal

association cortex; VL, ventrolateral thalamic nucleus; VM, ventromedial thalamic nucleus; VO, ventral orbital cortex.

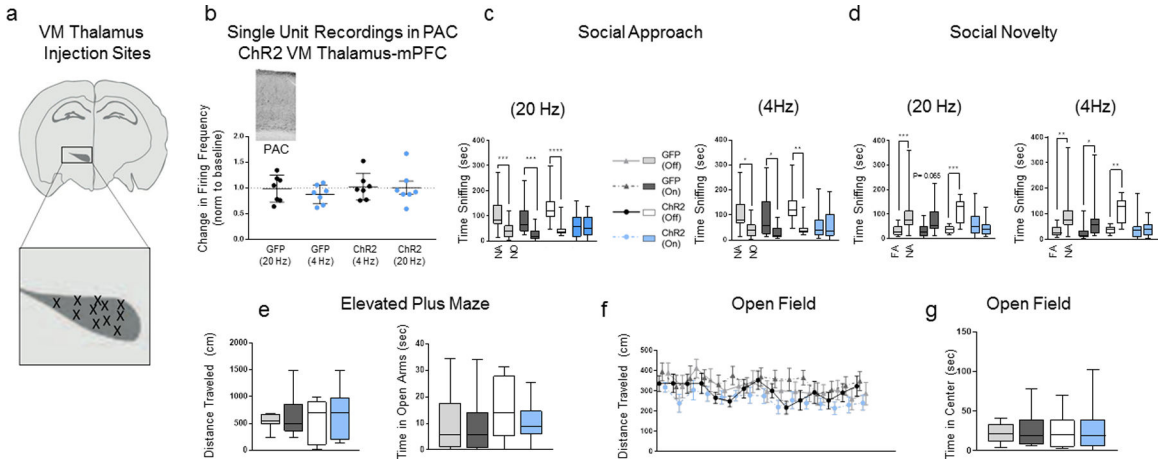

Extended Data Fig. 6. ChR2 activation of VM thalamus-PRL mPFC circuit.

a, Sample injection site locations for ChR2/Arch injection into the left VM thalamus. **b**, To test for possible antidromic activation, *in vivo* anesthetized single unit recordings in the VM thalamus-targeted parietal association cortex (PAC) were performed upon mPFC laser stimulation of ChR2 or GFP VM-thalamus terminals at 20 Hz or 4 Hz. Image of TdTomato positive terminals in PAC from LN AAV-1 tracing injection (top left). **c**, Three chambered social approach assay; time spent sniffing novel animal (NA), or novel object (NO) with 20 Hz (left) or 4 Hz (right) stimulation. **d**, Three chambered social novelty testing; time spent sniffing NA, or familiar animal (FA) with 20 Hz (left) or 4 Hz (right) stimulation. **e**, Time in the open arm and distance traveled in the elevated plus maze assay. **f**, Distance traveled in the open field and **g**, time in the center of the open field. All behavioral tests were analyzed with two or three-way ANOVA and Sidak post test and recordings were analyzed with two way ANOVA (unmarked = not significant). For frequency of spiking shown in figures as normalized values (mean SEM), raw values can be found in Extended Data Fig. 10. Box line denoted median/whiskers denoted 5–95%. n ≥ 10 for all behavioral experiments. ****$P <$ 0.0001; ***$P < 0.001$; **$P < 0.01$; *$P < 0.05$. P values and complete animal numbers can be found in Supplementary Table 2.

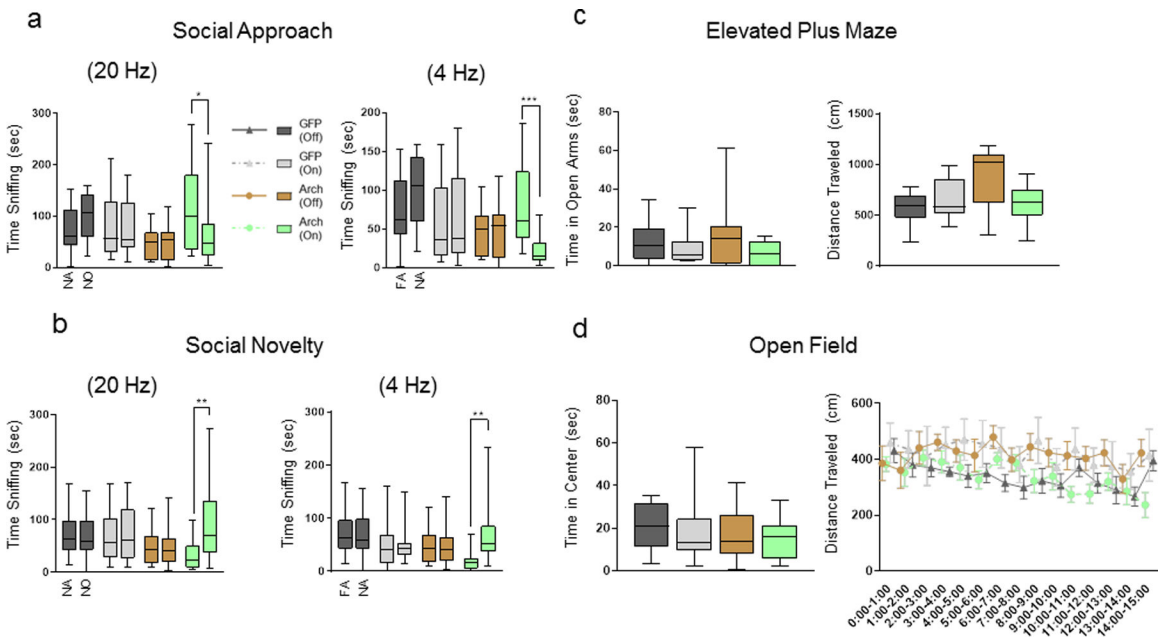

Extended Data Fig. 7. Arch inhibition of VM thalamus-PRL mPFC circuit on PC-Tsc1 mutant mice.

a, Three chambered social approach assay; time spent sniffing novel animal (NA), or novel object (NO) with 20 Hz (left) or 4 Hz (right) stimulation. **b**, Three chambered social novelty testing; time spent sniffing NA, or familiar animal (FA) with 20 Hz (left) or 4 Hz (right) stimulation. **c**, Time in the open arm and distance traveled in the elevated plus maze assay. **d**, Time in the center of the open field and distance traveled in the open field. All behavioral tests were analyzed with two or three-way ANOVA and Sidak post test. Box line denoted median/whiskers denoted 5–95%. N ≥ 10 for all behavioral experiments. ****$P < 0.0001$; ***$P < 0.001$; **$P < 0.01$; *$P < 0.05$. P values and complete animal numbers can be found in Supplementary Table 2.

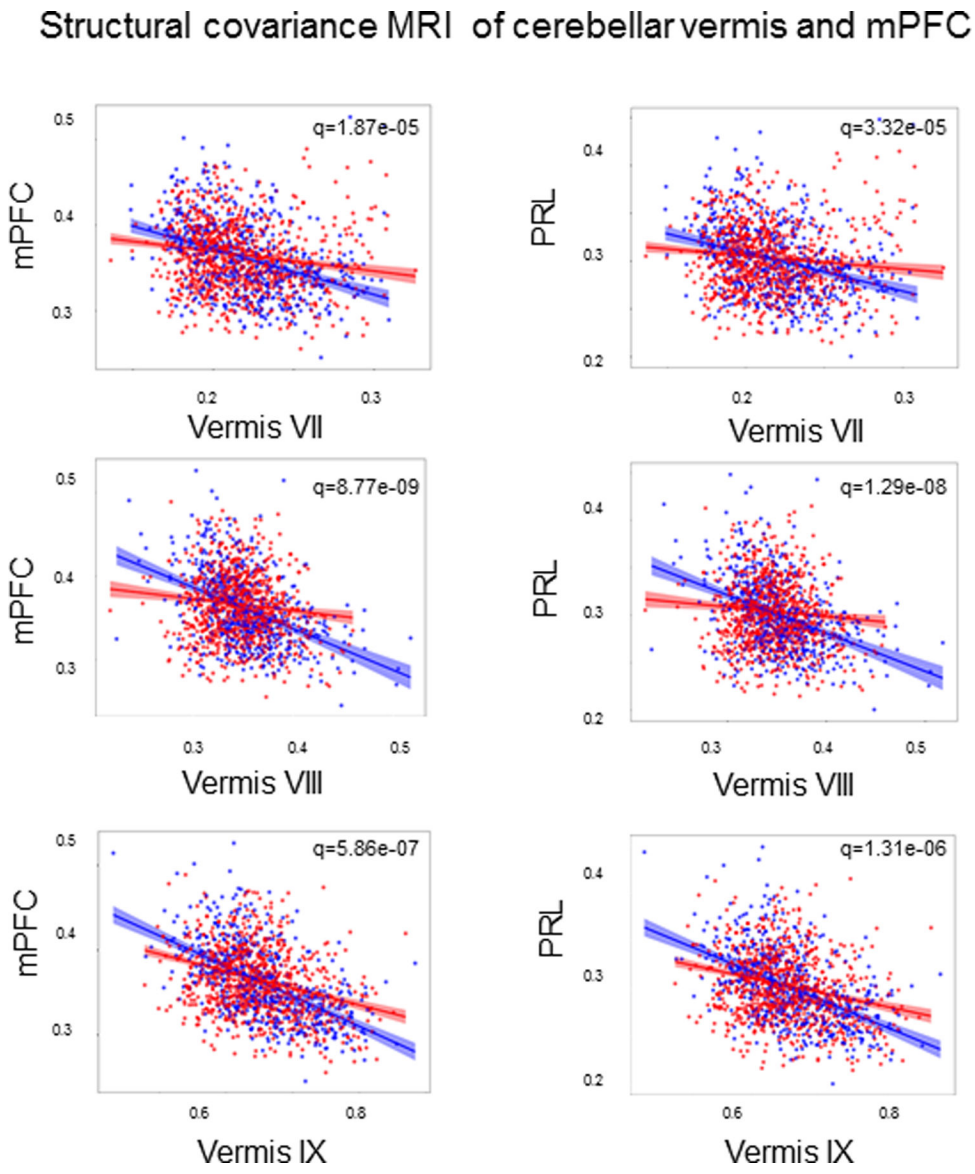

Extended Data Fig. 8. Structural covariance MRI of cerebellar vermis and mPFC.

Structural covariance MRI in mouse models of ASD vs. controls. Comparisons between vermis lobule VII (top), VIII (middle) or IX (bottom) and mPFC (left) or Prelimbic (PRL) mPFC (right). q values are stated. Each dot represents single imaged brain. Additional demographic information can be found in Supplementary Table 3.

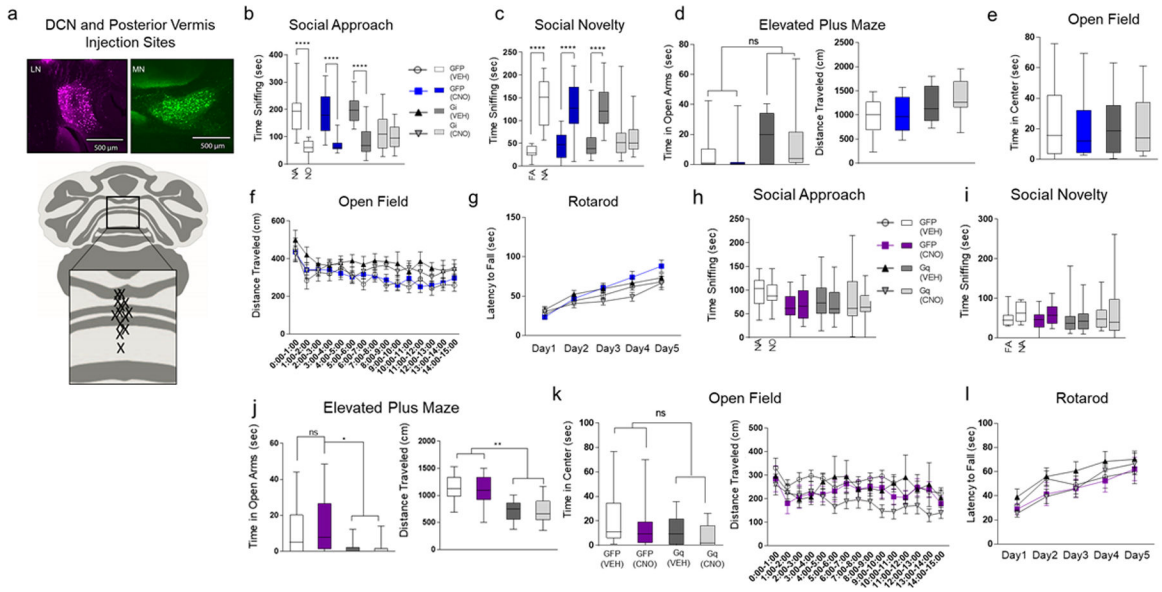

Extended Data Fig. 9. Gi DREADDs inhibition of PCs in the posterior vermis and Gq DREADDs activation of posterior vermis in PC-Tsc1 mutant mice.

a, Injection sites from MN and LN tracing to VM thalamus (top) and sample locations of Gi (inhibitory) or Gq (excitatory) DREADD injections into posterior vermis of PC-*Tsc1* mice (bottom). **b**, Three chambered social approach assay; time spent sniffing novel animal (NA), or novel object (NO). **c**, Three chambered social novelty testing; time spent sniffing NA, or familiar animal (FA). **d**, Time in the open arm and **e**, distance traveled in the elevated plus maze assay. **f**, Time in the center of the open field and **g**, distance traveled in the open field. **h**, Latency to fall in accelerating rotarod test. **i**, Three chambered social approach assay; time spent sniffing novel animal (NA), or novel object (NO). **j**, Three chambered social novelty testing; time sniffing novel animal (NA), or familiar animal (FA). **k**, Time in the open arm and distance traveled in the elevated plus maze assay. **l**, Time in the center of the open field and distance traveled in the open field. **m**, Latency to fall in accelerating rotarod test. All behavioral tests were analyzed with two or three-way ANOVA and Sidak post test. Box line denoted median/whiskers denoted 5–95%. n ≥ 10 for all behavioral tests. ****$P <$ 0.0001; ***$P <$ 0.001; **$P <$ 0.01; *$P <$ 0.05. P values and complete animal numbers can be found in Supplementary Table 2.

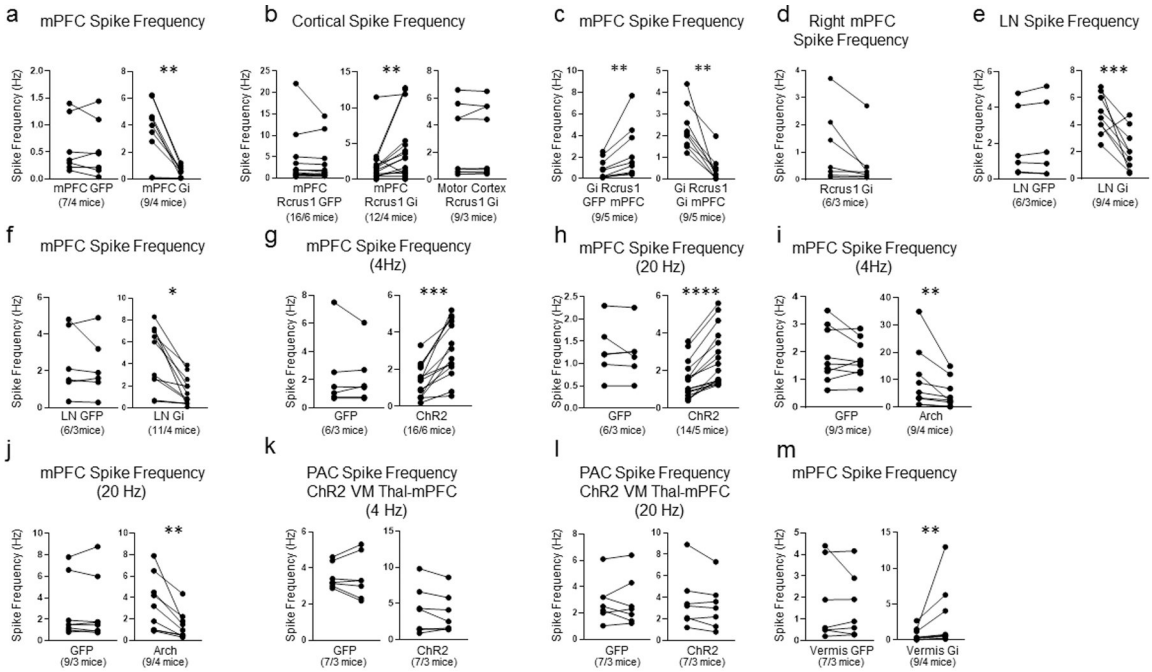

Extended Data Fig. 10. Raw frequency values for all normalized single unit graphs.

a, Frequency of firing of single units recorded in the left medial prefrontal cortex (mPFC) with control or inhibitory (Gi) DREADDs. **b**, Frequency of firing recorded in the left mPFC or motor cortex, with Rcrus1 Gi inhibition. **c**, Spike frequency in the mPFC with Rcrus1 Gi and mPFC Gi inhibition. **d**, Right mPFC spike frequency with Rcrus1 Gi. **e**, Spike Frequency in the Lateral Nucleus (LN) with LN Gi inhibition. **f**, mPFC spike frequency with LN Gi DREADDs. **g**, mPFC spike frequency with VM thalamic-mpfc Channel Rhodopsin (ChR2) activation of 4 Hz or **h**, 20 Hz. **i**, mPFC spike frequency with VM thalamus-mPFC Archaerhodopsin (Arch) inhibition at 4 Hz or **j**, 20 Hz. **k**, Parietal Association Cortex (PAC) firing with VM thalamic-mPFC ChR2 stimulation at 4 Hz and **l**, 20 Hz. **m**, mPFC spike frequency with posterior vermis Gi inhibition. ****$P < 0.0001$; ***$P < 0.001$; **$P < 0.01$; *$P < 0.05$. P values complete animal numbers can be found in Supplementary Table 2. Statistical analysis was done with the Wilcoxon matched pairs signed ranks test.

Supplementary Material

Refer to Web version on PubMed Central for supplementary material.

Acknowledgements

P.T.T. acknowledges support from the National Institute of Neurologic Disorders and Stroke (NS083733), the National Institute of Mental Health (MH116882), the Tuberous Sclerosis Alliance and the Department of Defense. E.K. acknowledges support from National Institute of Neurologic Disorders and Stroke (NS107004) and Autism Speaks. H.F. and S.d.L. acknowledge support from the National Institute of Neurologic Disorders and Stroke (NS095232 and NS105039). F. Morgado, J.E. and J.P.L. acknowledge support from the Canadian Institute for Health Research and the Ontario Brain Institute. L.C.R and C.J.S. acknowledge support from the National Institute for Health (MH106957). M.A.B. acknowledges support from the Medical Research Council (MR/K022377/1). N.K. acknowledges support from the National Institute of Mental Health (MH094268) and declares that he is a paid consultant for Rescindo Therapeutics, although this does not provide a competing interest with this study. P.T.T. and

E.K. acknowledge support from V. Jakkamsetti and J. Pascual for support with in vivo extracellular and acute slice recordings recordings and analysis; S. Birnbaum for assistance in behavioral studies; G. Konopka, C. Powell, L. Osburne, J. Foster, J. Lai, K. Rilett, E. Kim and A. Raznahan for generous provision of animal models; and J. Chadwick for graphics assistance.

References

1. D'Mello AM & Stoodley CJ Cerebro-cerebellar circuits in autism spectrum disorder. Front. Neurosci 9, 408 (2015). [PubMed: 26594140]
2. Fatemi SH et al. Consensus paper: pathological role of the cerebellum in autism. Cerebellum 11, 777–807 (2012). [PubMed: 22370873]
3. Mosconi MW, Wang Z, Schmitt LM, Tsai P & Sweeney JA The role of cerebellar circuitry alterations in the pathophysiology of autism spectrum disorders. Front. Neurosci 9, 296 (2015). [PubMed: 26388713]
4. Tsai PT Autism and cerebellar dysfunction: evidence from animal models. Semin. Fetal Neonatal Med 21, 349–355 (2016). [PubMed: 27179922]
5. Tsai PT et al. Autistic-like behaviour and cerebellar dysfunction in Purkinje cell Tsc1 mutant mice. Nature 488, 647–651 (2012). [PubMed: 22763451]
6. Pierce K & Courchesne E Evidence for a cerebellar role in reduced exploration and stereotyped behavior in autism. Biol. Psychiatry 49, 655–664 (2001). [PubMed: 11313033]
7. D'Mello AM, Crocetti D, Mostofsky SH & Stoodley CJ Cerebellar gray matter and lobular volumes correlate with core autism symptoms. Neuroimage Clin. 7, 631–639 (2015). [PubMed: 25844317]
8. Stoodley CJ et al. Altered cerebellar connectivity in autism and cerebellar-mediated rescue of autism-related behaviors in mice. Nat. Neurosci 20, 1744–1751 (2017). [PubMed: 29184200]
9. Krienen FM & Buckner RL Segregated fronto-cerebellar circuits revealed by intrinsic functional connectivity. Cereb. Cortex 19, 2485–2497 (2009). [PubMed: 19592571]
10. Middleton FA & Strick PL Cerebellar projections to the prefrontal cortex of the primate. J. Neurosci 21, 700–712 (2001). [PubMed: 11160449]
11. Van Overwalle F & Marien P Functional connectivity between the cerebrum and cerebellum in social cognition: a multi-study analysis. Neuroimage 124, 248–255 (2015). [PubMed: 26348560]
12. Watson TC, Becker N, Apps R & Jones MW Back to front: cerebellar connections and interactions with the prefrontal cortex. Front. Syst. Neurosci 8, 4 (2014). [PubMed: 24550789]
13. Steriade M Two channels in the cerebellothalamocortical system. J. Comp. Neurol 354, 57–70 (1995). [PubMed: 7615875]
14. Hazlett HC et al. Early brain development in infants at high risk for autism spectrum disorder. Nature 542, 348–351 (2017). [PubMed: 28202961]
15. Dichter GS Functional magnetic resonance imaging of autism spectrum disorders. Dialogues Clin. Neurosci 14, 319–351 (2012). [PubMed: 23226956]
16. Gilbert SJ, Meuwese JD, Towgood KJ, Frith CD & Burgess PW Abnormal functional specialization within medial prefrontal cortex in high-functioning autism: a multi-voxel similarity analysis. Brain 132, 869–878 (2009). [PubMed: 19174370]
17. Rogers TD et al. Connecting the dots of the cerebro-cerebellar role in cognitive function: neuronal pathways for cerebellar modulation of dopamine release in the prefrontal cortex. Synapse 65, 1204–1212 (2011). [PubMed: 21638338]
18. Rogers TD et al. Reorganization of circuits underlying cerebellar modulation of prefrontal cortical dopamine in mouse models of autism spectrum disorder. Cerebellum 12, 547–556 (2013). [PubMed: 23436049]
19. Buckner RL, Krienen FM, Castellanos A, Diaz JC & Yeo BT The organization of the human cerebellum estimated by intrinsic functional connectivity. J. Neurophysiol 106, 2322–2345 (2011). [PubMed: 21795627]
20. Gilbert SJ, Bird G, Brindley R, Frith CD & Burgess PW Atypical recruitment of medial prefrontal cortex in autism spectrum disorders: an fMRI study of two executive function tasks. Neuropsychologia 46, 2281–2291 (2008). [PubMed: 18485420]

21. Pirone A et al. Social stimulus causes aberrant activation of the medial prefrontal cortex in a mouse model with autism-like behaviors. Front. Synaptic Neurosci 10, 35 (2018). [PubMed: 30369876]
22. Kobayashi M, Hayashi Y, Fujimoto Y & Matsuoka I Decreased parvalbumin and somatostatin neurons in medial prefrontal cortex in BRINP1-KO mice. Neurosci. Lett 683, 82–88 (2018). [PubMed: 29960053]
23. Yizhar O et al. Neocortical excitation/inhibition balance in information processing and social dysfunction. Nature 477, 171–178 (2011). [PubMed: 21796121]
24. Selimbeyoglu A et al. Modulation of prefrontal cortex excitation/inhibition balance rescues social behavior in CNTNAP2-deficient mice. Sci. Transl. Med 9, eaah6733 (2017). [PubMed: 28768803]
25. Alexander-Bloch A, Giedd JN & Bullmore E Imaging structural co-variance between human brain regions. Nat. Rev. Neurosci 14, 322–336 (2013). [PubMed: 23531697]
26. Baribeau DA et al. Structural neuroimaging correlates of social deficits are similar in autism spectrum disorder and attention-deficit/hyperactivity disorder: analysis from the POND. Netw. Transl. Psychiatry 9, 72 (2019).
27. Jansen J & Brodal AExperimental studies on the intrinsic fibers of the cerebellum II. The cortico-nuclear projection. Cerebellum 10, 126–180 (1940).
28. Zingg B et al. AAV-mediated anterograde transsynaptic tagging: mapping corticocollicular input-defined neural pathways for defense behaviors. Neuron 93, 33–47 (2017). [PubMed: 27989459]
29. Kuramoto E et al. Ventral medial nucleus neurons send thalamocortical afferents more widely and more preferentially to layer 1 than neurons of the ventral anterior-ventral lateral nuclear complex in the rat. Cereb. Cortex 25, 221–235 (2015). [PubMed: 23968832]
30. Mitchell BD & Cauller LJ Corticocortical and thalamocortical projections to layer I of the frontal neocortex in rats. Brain Res. 921, 68–77 (2001). [PubMed: 11720712]
31. Urbain N, Fourcaud-Trocme N, Laheux S, Salin PA & Gentet LJ Brain-state-dependent modulation of neuronal firing and membrane potential dynamics in the somatosensory thalamus during natural sleep. Cell Rep. 26, 1443–1457 (2019). [PubMed: 30726730]
32. Badura A et al. Normal cognitive and social development require posterior cerebellar activity. eLife. 7, e36401 (2018). [PubMed: 30226467]
33. Srivastava S et al. Volumetric analysis of the basal ganglia and cerebellar structures in patients with Phelan–McDermid syndrome. Pediatr. Neurol 90, 37–43 (2019). [PubMed: 30396833]
34. Courville J & Diakiw N Cerebellar corticonuclear projection in the cat. The vermis of the anterior and posterior lobes. Brain Res. 110, 1–20 (1976). [PubMed: 1276942]
35. Groenewegen HJ Organization of the afferent connections of the mediodorsal thalamic nucleus in the rat, related to the mediodorsal-prefrontal topography. Neuroscience 24, 379–431 (1988). [PubMed: 2452377]
36. Haroian AJ, Massopust LC & Young PA Cerebellothalamic projections in the rat: an autoradiographic and degeneration study. J. Comp. Neurol 197, 217–236 (1981). [PubMed: 7276233]
37. Rubenstein JL & Merzenich MM Model of autism: increased ratio of excitation/inhibition in key neural systems. Genes Brain Behav. 2, 255–267 (2003). [PubMed: 14606691]
38. Takarae Y & Sweeney J Neural hyperexcitability in autism spectrum disorders. Brain Sci. 7, 129 (2017).
39. Contractor A, Klyachko VA & Portera-Cailliau C Altered neuronal and circuit excitability in fragile X syndrome. Neuron 87, 699–715 (2015). [PubMed: 26291156]
40. Sohal VS, Zhang F, Yizhar O & Deisseroth K Parvalbumin neurons and gamma rhythms enhance cortical circuit performance. Nature 459, 698–702 (2009). [PubMed: 19396159]
41. Mouginot D & Gahwiler BH Characterization of synaptic connections between cortex and deep nuclei of the rat cerebellum in vitro. Neuroscience 64, 699–712 (1995). [PubMed: 7715782]
42. Ryu YH et al. Perfusion impairments in infantile autism on technetium-99m ethyl cysteinate dimer brain single-photon emission tomography: comparison with findings on magnetic resonance imaging. Eur. J. Nucl. Med 26, 253–259 (1999). [PubMed: 10079316]
43. Carta I, Chen CH, Schott AL, Dorizan S & Khodakhah K Cerebellar modulation of the reward circuitry and social behavior. Science 363, eaav0581 (2019). [PubMed: 30655412]

44. Bicks LK, Koike H, Akbarian S & Morishita H Prefrontal cortex and social cognition in mouse and man. Front. Psychol 6, 1805 (2015). [PubMed: 26635701]
45. Popa LS & Ebner TJ Cerebellum, predictions and errors. Front. Cell Neurosci 12, 524 (2018). [PubMed: 30697149]
46. Carmi L et al. Clinical and electrophysiological outcomes of deep TMS over the medial prefrontal and anterior cingulate cortices in OCD patients. Brain Stimulation 11, 158–165 (2018). [PubMed: 28927961]
47. van Dun K, Bodranghien F, Manto M & Marien P Targeting the cerebellum by noninvasive neurostimulation: a review. Cerebellum 16, 695–741 (2017). [PubMed: 28032321]
48. Parker KL et al. Delta-frequency stimulation of cerebellar projections can compensate for schizophrenia-related medial frontal dysfunction. Mol. Psychiatry 22, 647–655 (2017). [PubMed: 28348382]
49. Brady RO Jr. et al. Cerebellar-prefrontal network connectivity and negative symptoms in schizophrenia. Am. J. Psychiatry 176, 512–520 (2019). [PubMed: 30696271]
50. Tsai PT et al. Sensitive periods for cerebellar-mediated autistic-like behaviors. Cell Rep. 25, 357–367 (2018). [PubMed: 30304677]
51. Barski JJ, Dethleffsen K & Meyer M Cre recombinase expression in cerebellar Purkinje cells. Genesis 28, 93–98 (2000). [PubMed: 11105049]
52. Kwiatkowski DJ et al. A mouse model of TSC1 reveals sex-dependent lethality from liver hemangiomas, and up-regulation of p70S6 kinase activity in Tsc1 null cells. Hum. Mol. Genet 11, 525–534 (2002). [PubMed: 11875047]
53. Madisen L et al. A robust and high-throughput Cre reporting and characterization system for the whole mouse brain. Nat. Neurosci 13, 133–140 (2009). [PubMed: 20023653]
54. Paxinos G & Franklin K Paxinos and Franklin's the Mouse Brain in Stereotaxic Coordinates 4th edn (Academic Press, 2012).
55. Watson C, Paxinos G & Puelles L The Mouse Nervous System (Academic Press, 2011).
56. Armbruster BN, Li X, Pausch MH, Herlitze S & Roth BL Evolving the lock to fit the key to create a family of G protein-coupled receptors potently activated by an inert ligand. Proc. Natl Acad. Sci. USA 104, 5163–5168 (2007). [PubMed: 17360345]
57. Cahill LS et al. Preparation of fixed mouse brains for MRI. Neuroimage 60, 933–939 (2012). [PubMed: 22305951]
58. Lerch JP, Sled JG & Henkelman RM MRI phenotyping of genetically altered mice. Methods Mol. Biol 711, 349–361 (2011). [PubMed: 21279611]
59. Nieman BJ et al. MR technology for biological studies in mice. NMR Biomed. 20, 291–303 (2007). [PubMed: 17451169]
60. Nieman BJ et al. Magnetic resonance imaging for detection and analysis of mouse phenotypes. NMR Biomed. 18, 447–468 (2005). [PubMed: 16206127]
61. Nieman BJ, Flenniken AM, Adamson SL, Henkelman RM & Sled JG Anatomical phenotyping in the brain and skull of a mutant mouse by magnetic resonance imaging and computed tomography. Physiological Genomics 24, 154–162 (2006). [PubMed: 16410543]
62. Dazai J et al. Multiple mouse biological loading and monitoring system for MRI. Magn. Reson. Med 52, 709–715 (2004). [PubMed: 15389955]
63. Dazai J, Spring S, Cahill LS & Henkelman RM Multiple-mouse neuroanatomical magnetic resonance imaging. J. Vis. Exp 48, 2497 (2011).
64. Thomas DL et al. High-resolution fast spin echo imaging of the human brain at 4.7T: implementation and sequence characteristics. Magn. Reson. Med 51, 1254–1264 (2004). [PubMed: 15170847]
65. Nieman BJ et al. Fast spin-echo for multiple mouse magnetic resonance phenotyping. Magn. Reson. Med 54, 532–537 (2005). [PubMed: 16086298]
66. Dorr AE, Lerch JP, Spring S, Kabani N & Henkelman RM High resolution three-dimensional brain atlas using an average magnetic resonance image of 40 adult C57Bl/6J mice. Neuroimage 42, 60–69 (2008). [PubMed: 18502665]

67. Richards K et al. Segmentation of the mouse hippocampal formation in magnetic resonance images. Neuroimage 58, 732–740 (2011). [PubMed: 21704710]
68. Steadman PE et al. Genetic effects on cerebellar structure across mouse models of autism using a magnetic resonance imaging atlas. Autism Res. 7, 124–137 (2014). [PubMed: 24151012]
69. Ullmann JF, Watson C, Janke AL, Kurniawan ND & Reutens DC A segmentation protocol and MRI atlas of the C57BL/6J mouse neocortex. Neuroimage 78, 196–203 (2013). [PubMed: 23587687]
70. Chakravarty MM et al. Performing label-fusion-based segmentation using multiple automatically generated templates. Hum. Brain Mapp 34, 2635–2654 (2013). [PubMed: 22611030]
71. Park MT et al. Derivation of high-resolution MRI atlases of the human cerebellum at 3T and segmentation using multiple automatically generated templates. Neuroimage 95, 217–231 (2014). [PubMed: 24657354]
72. Kim JS et al. Automated 3-D extraction and evaluation of the inner and outer cortical surfaces using a Laplacian map and partial volume effect classification. Neuroimage 27, 210–221 (2005). [PubMed: 15896981]
73. Lerch JP & Evans AC Cortical thickness analysis examined through power analysis and a population simulation. Neuroimage 24, 163–173 (2005). [PubMed: 15588607]
74. Lyttelton O, Boucher M, Robbins S & Evans A An unbiased iterative group registration template for cortical surface analysis. Neuroimage 34, 1535–1544 (2007). [PubMed: 17188895]
75. Reardon PK et al. Normative brain size variation and brain shape diversity in humans. Science 360, 1222–1227 (2018). [PubMed: 29853553]
76. Roth BL DREADDs for neuroscientists. Neuron 89, 683–694 (2016). [PubMed: 26889809]
77. Deisseroth K Optogenetics: 10 years of microbial opsins in neuroscience. Nat. Neurosci 18, 1213–1225 (2015). [PubMed: 26308982]
78. Holmes A et al. Behavioral characterization of dopamine D_5 receptor null mutant mice. Behav. Neurosci 115, 1129 (2001). [PubMed: 11584926]
79. Buitrago MM, Schulz JB, Dichgans J & Luft AR Short and long-term motor skill learning in an accelerated rotarod training paradigm. Neurobiol. Learn. Mem 81, 211–216 (2004). [PubMed: 15082022]
80. Yang M, Silverman JL & Crawley JN Automated three-chambered social approach task for mice. Curr. Protoc. Neurosci 56, 8.26.21–28.26.16 (2011).
81. Silverman JL et al. Sociability and motor functions in Shank1 mutant mice. Brain Res. 1380, 120–137 (2011). [PubMed: 20868654]
82. Yang M & Crawley JN Simple behavioral assessment of mouse olfaction. Curr. Protoc. Neurosci 48, 8.24.1–8.24.12 (2009).
83. Bednar I et al. Selective nicotinic receptor consequences in APPSWE transgenic mice. Mol. Cell. Neurosci 20, 354–365 (2002). [PubMed: 12093166]

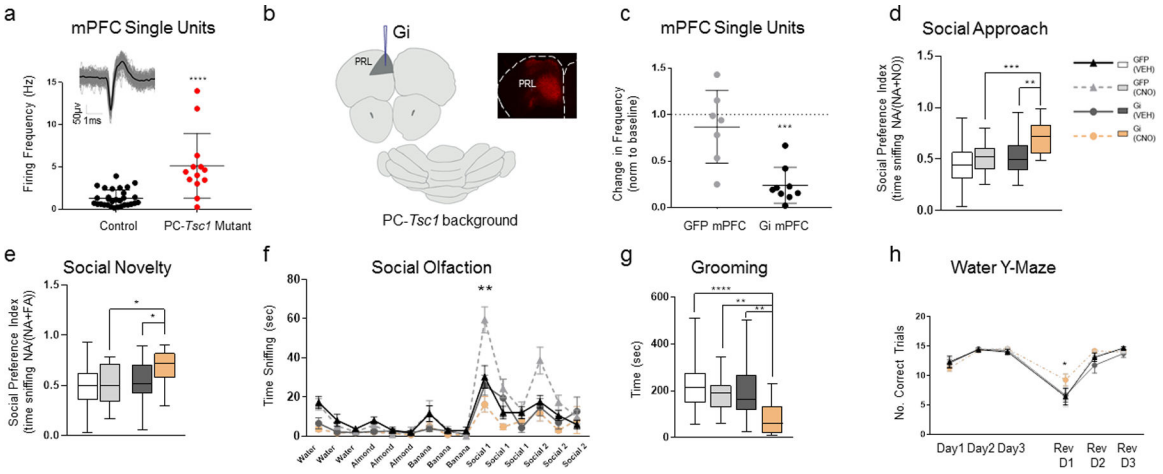

Fig. 1: Modulation of elevated PRL activity in PC-Tsc1 mutants rescues social deficits and repetitive/inflexible behaviors.

a, In vivo extracellular recordings in the left PRL mPFC in PC-*Tsc1* mutants and littermate controls. Average single-unit firing frequency, with superimposed single-unit traces (top) with average and summary trace (thick black line). **b**, Representative injection site of inhibitory Gi DREADDs into the left PRL mPFC of PC-*Tsc1* mutants. **c**, Validation of inhibitory Gi DREADDs function through extracellular single-unit recordings in the left PRL of anesthetized mice. **d**,**e**, Three-chambered social approach assay and social index (**d**) and three-chambered social novelty assay and social index (**e**). **f**,**g**, Time spent sniffing scents in social olfaction assay (**f**) and time spent grooming (**g**). **h**, Behavioral flexibility tested in water Y-maze. Rev D, reversal day. All behavioral tests include Gi DREADD-injected and GFP-injected PC-*Tsc1* mutants with both CNO and VEH conditions. Box line denotes median, and whiskers denote 5–95%. $n \geq 10$ for all groups. Mann–Whitney test conducted for recording analysis, shown as mean ± s.e.m. All raw values for frequency of spiking (shown in figures as normalized values) can be found in Extended Data Fig. 10. Two-way ANOVA with Sidak's post test used for all behavioral tests. ****$P < 0.0001$, ***$P < 0.001$, **$P < 0.01$ and *$P < 0.05$. All other comparisons are not significant. Complete P values and animal numbers can be found in Supplementary Table 1.

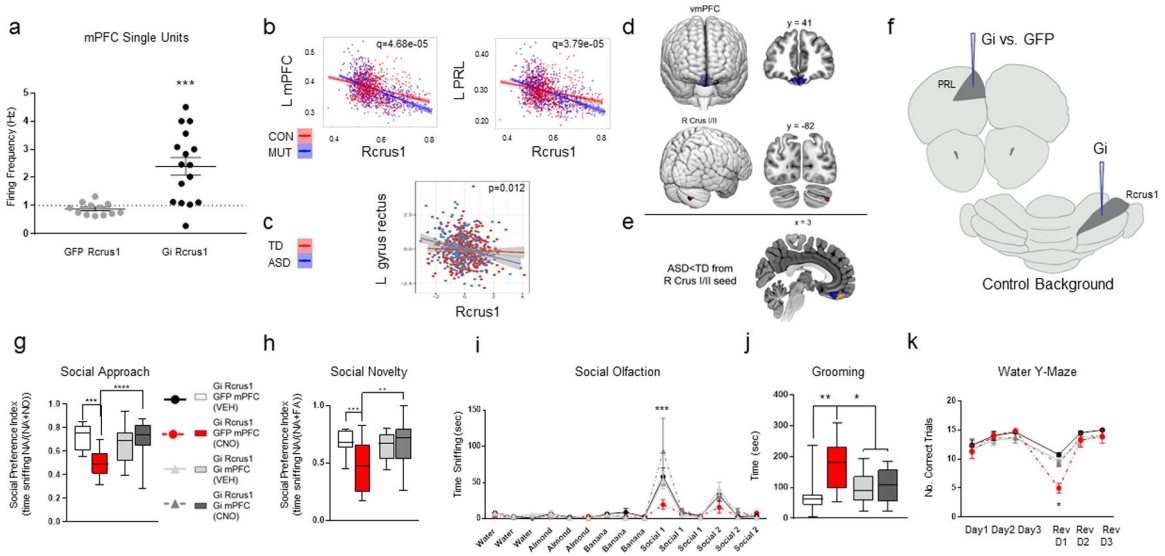

Fig. 2: Rcrus1 and PRL are functionally connected and play important roles in ASD behaviors.

a, Average single-unit frequency in the left PRL mPFC upon chemogenetic inhibition of Rcrus1. **b**, Structural MRI covariance between Rcrus1 and left mPFC (left) and PRL (right) across 30 mouse models of ASD-linked genes; FDR-corrected *q* values. **c**, Structural MRI covariance between Rcrus1 and left gyrus rectus in human TD and ASD cohorts from the POND study. For **b** and **c**, each dot represents a single imaged brain. **d**,**e**, Functional MRI MVPA similarly reveals altered functional connectivity in the mPFC and Rcrus1 and Rcrus2 in individuals with ASD ($P < 0.001$, FDR cluster $P < 0.05$) (**d**), whereas post hoc seed-to-voxel analyses from Rcrus1 seed reveals reduced functional connectivity with the mPFC (yellow), which overlaps with the region delineated by the MVPA (blue) ($P < 0.001$, $k > 50$) and with structural MRI findings (**e**). vmPFC, ventromedial PFC. **f**, Diagram of experimental approach for viral injections into PRL and Rcrus1. **g**–**k**, Effect of PRL inhibition on Rcrus1 inhibition-mediated ASD behaviors. **g**, Social index from three-chambered social approach **h**, Social novelty testing. **i**,**j**, Time spent sniffing in social olfaction assay (**i**) and time spent grooming (**j**) were tested. **k**, Behavioral flexibility tested in water Y-maze assay. All behavioral tests include mice with Gi DREADDs injected into Rcrus1 and either Gi DREADDs or GFP injected into the mPFC with either VEH or CNO injections. Box line denotes median, and whiskers denote 5–95% range. $n \geq 10$ for all groups. Mann–Whitney test conducted for recording analysis, shown as mean ± s.e.m. All raw values for frequency of spiking (shown in figures as normalized values) can be found in Extended Data Fig. 10. Two-way ANOVA with Sidak's post test used for all behavioral tests. All unlabeled comparisons are not significant. ****$P < 0.0001$, ***$P < 0.001$, **$P < 0.01$ and *$P < 0.05$. *P* values, *q* values and complete numbers and demographics can be found in Supplementary Tables 1, 3 and 4. CON, control; MUT, mutant.

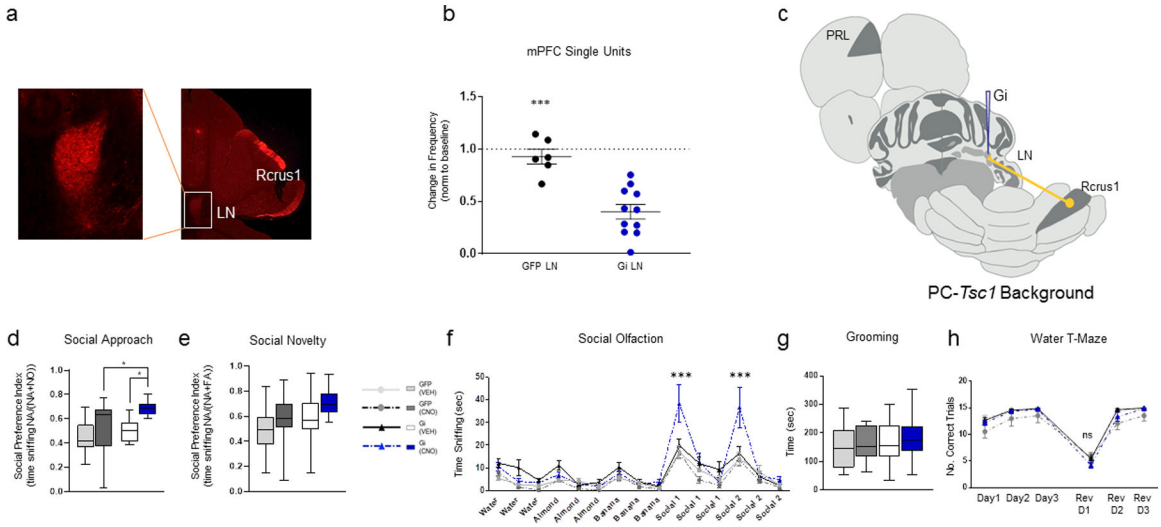

Fig. 3: The cerebellar LN is functionally connected to the PRL cortex and regulates social behaviors.

a, PCs in Rcrus1 project predominantly to the right LN. **b**, PRL single-unit firing with Gi DREADDs suppression of LN. **c**, Diagram of experimental approach for Gi DREADDs injection into the LN of PC-*Tsc1* mutant mice. **d**–**h**, Effect of chemogenetic inhibition of right LN (Gi DREADD) on ASD behaviors in PC-*Tsc1* mutant mice. **d**,**e**, Social index from the three-chambered social approach assay (**d**) and social index from social novelty testing (**e**). **f**,**g**, Time spent sniffing in social olfaction assay (**f**) and time spent grooming (**g**) were tested. **h**, Behavioral flexibility tested in water Y-maze assay. Box line denotes median, and whiskers denote 5–95%. $n \geq 9$ for all groups. Mann–Whitney test conducted for recording analysis, shown as mean ± s.e.m. All raw values for frequency of spiking (shown in figures as normalized values) can be found in Extended Data Fig. 10. Two-way ANOVA with Sidak's post test used for all behavioral tests. All unlabeled comparisons are not significant. ****$P < 0.0001$, ***$P < 0.001$, **$P < 0.01$ and *$P < 0.05$. P values, q values and complete animal numbers can be found in Supplementary Table 1.

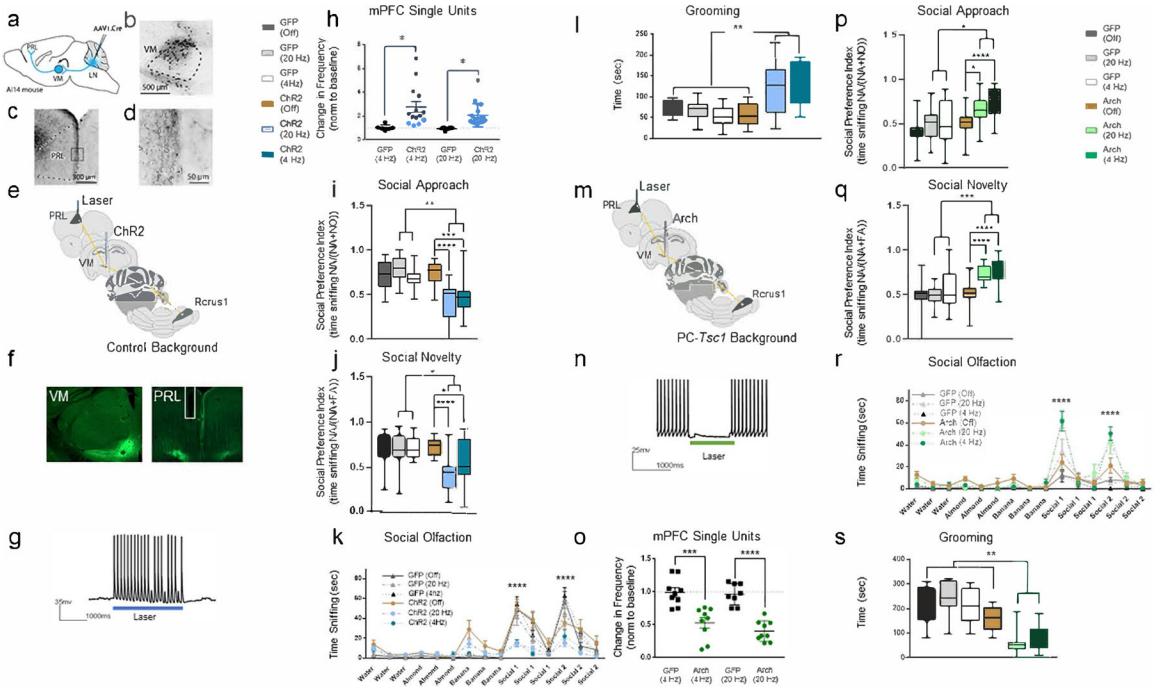

Fig. 4: VM thalamus connects to the PRL cortex to regulate ASD behaviors.

a, Trans-synaptic anterograde AAV-1^{Cre} injected into the LN of Cre-dependent Td-tomato reporter mice. **b**–**d**, Labeling of postsynaptic neuronal cell bodies was observed in the left VM thalamus and terminals in the left PRL mPFC. **e**,**f**, Diagram of experimental approach for ChR2 experiments (**e**) and representative injection site in thalamus and optical fiber placement for optogenetic experiments (**f**). **g**, ChR2 stimulation of VM thalamic cells in acute slice preparations results in increased spiking. **h**, Single units from extracellular recordings in the left PRL mPFC upon 20-Hz or 4-Hz laser stimulation of thalamic-derived terminals in the PRL mPFC. **i**–**l**, Effect of optogenetic activation (4 Hz or 20 Hz) of VM thalamic terminals in the PRL cortex on behavior. **i**,**j**, Social index from the three-chambered social approach assay (**i**) and social index from the social novelty testing (**j**). **k**,**l**, Time spent sniffing in social olfaction assay (**k**) and time spent grooming (**l**) were tested. **m**, Experimental approach for Arch experiments. **n**, Patch-clamp recordings in acute slice preparations of mice injected with AAV-Arch into the VM thalamus, showing inhibition of thalamic cell firing with photic activation. **o**, Change in single-unit frequency in the left PRL mPFC upon optogenetic stimulation of VM thalamus-derived terminals in the PRL. **p**–**s**, Effect of optogenetic inhibition (4 Hz or 20 Hz) of VM thalamic terminals in the PRL cortex on ASD behaviors seen in PC-*Tsc1* mutant mice. **p**,**q**, Social index from three-chambered social approach assay (**p**) and social novelty testing (**q**). **r**,**s**, Time spent sniffing in social olfaction assay (**r**) and time spent grooming (**s**) were tested. Box line denotes median, and whiskers denote 5–95%. $n \geq 10$ for all groups. Two-way ANOVA conducted for recording analysis, shown as mean ± s.e.m. All raw values for frequency of spiking (shown in figures as normalized values) can be found in Extended Data Fig. 10. Two-way ANOVA with Sidak's post test used for all behavioral tests. All unlabeled comparisons are not significant. ****$P < 0.0001$, ***$P < 0.001$, **$P < 0.01$ and *$P < 0.05$. P values and complete animal numbers can be found in Supplementary Table 1.

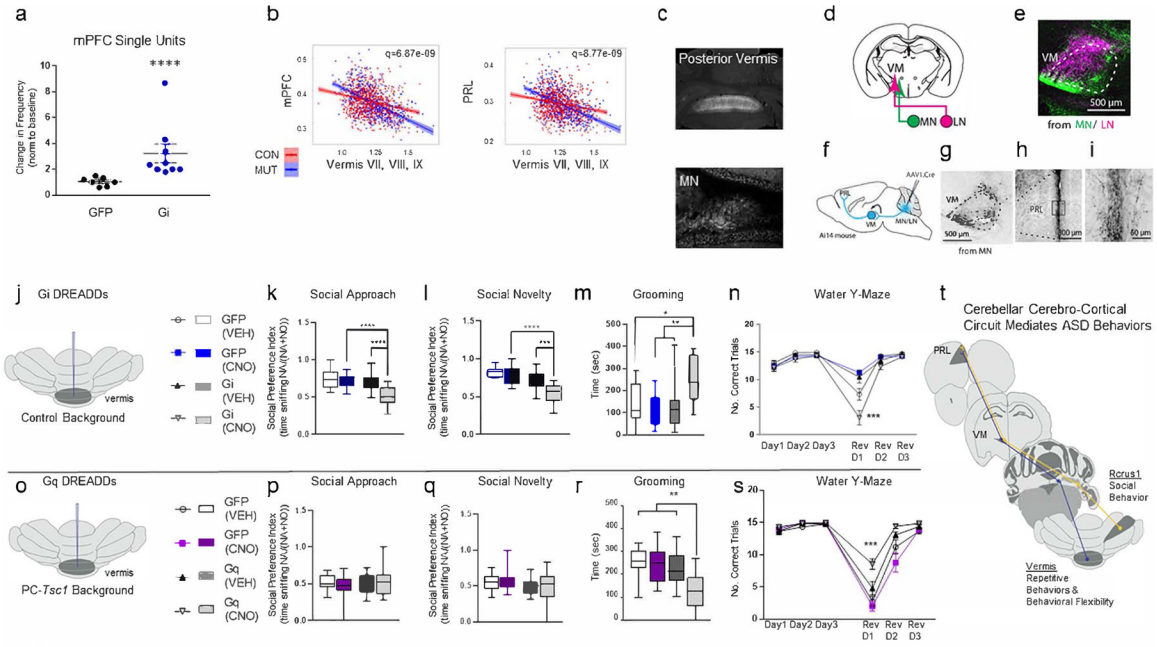

Fig. 5: Posterior cerebellar vermis is structurally and functionally connected to PRL, and stimulation specifically rescues repetitive/inflexible behaviors.

a, Change in single-unit firing frequency in the mPFC upon chemogenetic inhibition (Gi) of posterior vermis PCs. **b**, MRI reveals altered structural covariance between posterior vermis and mPFC (left) PRL area (right) in 30 mouse models of ASD-linked genes. Each dot represents a single imaged brain. **c**, Cerebellar vermis PCs project predominantly to the MN. MN and LN both project to the VM thalamus. **d**,**e**, Viral injections into LN (pink) and MN (green) both reveal terminals in the VM thalamus. **f**–**i**, Trans-synaptic AAV-1^{Cre} anterograde tracing injected into the MN of Cre-dependent Td-tomato reporter mice reveals postsynaptic cells in the VM thalamus (**f**,**g**) and terminals in the left PRL mPFC (**h**,**i**). **j**–**n**, Effect of chemogenetic inhibition (Gi) of posterior vermis (**j**) on ASD behavior (**k**–**n**). **k**,**l**. Social index from the three-chambered social approach assay (**k**) and social index from the social novelty assay (**l**). **m**, Time spent grooming was tested. **n**, Behavioral flexibility was tested in water Y-maze assay. Rev D, reversal day. **o**–**s**, Effect of chemogenetic stimulation (Gq) of posterior vermis (**o**) on ASD behaviors in PC-*Tsc1* mutant mice (**p**–**s**). **p**,**q**, Social index from the three-chambered social approach assay (**p**) and social novelty assay (**q**). **r**, Time spent grooming was tested. **s**, Behavioral flexibility was tested in water Y-maze assay. **t**, Schematic of cerebellar cerebrocortical circuits regulated by Rcrus1 and posterior vermis. Box line denotes median, and whiskers denote 5–95%. $n \geq 9$ for all groups. Mann–Whitney test conducted for recording analysis, shown as mean ± s.e.m. All raw values for frequency of spiking (shown in figures as normalized values) can be found in Extended Data Fig. 10. Two-way ANOVA with Sidak's post test used for all behavioral tests. All unlabeled comparisons are not significant. $P < 0.0001$, ***$P < 0.001$, **$P < 0.01$ and *$P < 0.05$. P values, q values and complete animal numbers can be found in Supplementary Tables 1 and 3. CON, control; MUT, mutant.